J. Fluid Mech. (2006), *vol.* 553, *pp.* 33–73.
doi:10.1017/S0022112006008640 Printed in the United Kingdom

An accurate and comprehensive model of thin fluid flows with inertia on curved substrates

By A. J. ROBERTS AND ZHENQUAN LI

Department of Mathematics and Computing, University of Southern Queensland, Toowoomba, Queensland 4350, Australia
aroberts@usq.edu.au; li_z@usp.ac.fj

(Received 30 January 2004 and in revised form 30 August 2005)

Consider the three-dimensional flow of a viscous Newtonian fluid upon a curved two-dimensional substrate when the fluid film is thin, as occurs in many draining, coating and biological flows. We derive a comprehensive model of the dynamics of the film, the model being expressed in terms of the film thickness η and the average lateral velocity $\bar{\boldsymbol{u}}$. Centre manifold theory assures us that the model accurately and systematically includes the effects of the curvature of substrate, gravitational body force, fluid inertia and dissipation. The model resolves wavelike phenomena in the dynamics of viscous fluid flows over arbitrarily curved substrates such as cylinders, tubes and spheres. We briefly illustrate its use in simulating drop formation on cylindrical fibres, wave transitions, three-dimensional instabilities, Faraday waves, viscous hydraulic jumps, flow vortices in a compound channel and flow down and up a step. These models are the most complete models for thin-film flow of a Newtonian fluid; many other thin-film models can be obtained by different restrictions and truncations of the model derived here.

1. Introduction

Mathematical models and numerical simulations for the flow of a thin film of fluid have important applications in industrial and natural processes (Roskes 1969; Ruschak 1985; Moriarty, Schwartz & Tuck 1991; Chang 1994; Grotberg 1994; Schwartz & Weidner 1995; Schwartz, Weidner & Eley 1995; Decré & Baret 2003). The dynamics of a thin fluid film spreading or retracting from the surface of a supporting liquid or solid substrate has long been an active area of research because of its impact on many technological fields: for example, applications of coating flows (Ruschak 1985) range from a single decorative layer on packaging, to multiple-layer coatings on photographic film; coated products include adhesive tape, surgical dressings, magnetic and optical recording media, lithographic plates, paper and fabrics. Oron, Davis & Bankoff (1997) reviewed a wide variety of thin fluid film models in detail. In this section, we summarize some of the results on mathematical models for three-dimensional thin fluid film flows on a solid curved substrate and relate these results to the new comprehensive model derived herein.

In a three-dimensional and very slow flow, a 'lubrication' model for the evolution of the thickness η of a film on a general curved substrate was shown by Roy, Roberts & Simpson (2002) (see also Howell 2003) to be

$$\frac{\partial \zeta}{\partial t} \approx -\tfrac{1}{3}\, We\, \nabla\cdot\left[\eta^2\zeta\nabla\tilde{\kappa} - \tfrac{1}{2}\eta^4(\kappa\boldsymbol{I}-\boldsymbol{K})\cdot\nabla\kappa\right], \tag{1}$$

where $\zeta = \eta - \frac{1}{2}\kappa\eta^2 + \frac{1}{3}k_1k_2\eta^3$ is proportional to the amount of fluid locally 'above' a small patch of the substrate; $\tilde{\kappa}$ is the mean curvature of the free surface of the film owing to both substrate and fluid thickness variations ($\tilde{\kappa} \approx \kappa + \nabla^2\eta$); $\boldsymbol{K}$ is the curvature tensor of the substrate; k_1, k_2 and $\kappa = k_1 + k_2$ are the principal curvatures and the mean curvature of the substrate, respectively (positive curvature is concave); the Weber number *We* characterizes the strength of surface tension; and the differential operator ∇ is defined in a coordinate system fitted to the curved substrate. Based upon a systematic analysis of the continuity and Navier–Stokes equations for a Newtonian fluid, this model accounts for any general curvature of the substrate and that of the surface of the film. Decré & Baret (2003) found good agreement between a linearized version of lubrication models such as (1) and experiments of flow over various shaped depressions in the substrate.

In many applications, the lubrication model, such as (1), of slow flow of a thin fluid film is too limited. Indeed, Pumir, Manneville & Pomeau (1983) and Ruyer-Quil & Manneville (2000) show that such lubrication models may have finite time singularities for moderate Reynolds numbers. Instead, as we develop here, a model expressed in terms of the dynamics of both the fluid layer thickness η and an overall lateral velocity $\bar{\boldsymbol{u}}$ (or momentum flux) is required to resolve faster wavelike dynamics in many situations: falling films (Nguyen & Balakotaiah 2000; Chang 1994, p. 110); wave transitions (Chang, Demekhin & Saprikin 2002) to solitary waves (Ruyer-Quil & Manneville 2000); higher Reynolds-number flows (Prokopiou, Cheng & Chang 1991, equation (19)); in rising film flow and a slot coater (Kheshgi 1989, equation (37)); and rivulets under a sloping cylinder (Alekseenko, Markovich & Shtork 1996). Oron *et al.* (1997, p. 975) comment that 'upgrading the importance of inertia has been shown to be crucial in the study of falling films'. Most of these models are only for two-dimensional flow, not the three-dimensional flow explored here. Roberts (1998) also derived a similar model for two-dimensional flow, approximately

$$\frac{\partial\eta}{\partial t} \approx -\frac{\partial(\eta\bar{u})}{\partial x}, \tag{2}$$

$$Re\,\frac{\partial\bar{u}}{\partial t} \approx -\left[\frac{\pi^2}{4}\frac{\bar{u}}{\eta^2} + 3\kappa\frac{\bar{u}}{\eta}\right] + \frac{\pi^2}{12}\left(We\,\frac{\partial\tilde{\kappa}}{\partial x} + Gr\,g_s\right), \tag{3}$$

where *Re* is a Reynolds number of the flow, $\bar{u}$ is the lateral velocity averaged over the fluid thickness, and $Gr\,g_s$ is the lateral component of gravity. Compare such a model and the lubrication model (1) for slow flows: in the simplest situation of two-dimensional flow on a flat substrate without gravity, the lubrication model (1) reduces to a nonlinear diffusion like equation $\eta_t = -\frac{1}{3}\,We(\eta^3\eta_{xxx})_x$; whereas models such as (2)–(3) reduce to

$$\frac{\partial\eta}{\partial t} \approx -\frac{\partial(\eta\bar{u})}{\partial x}, \quad Re\,\frac{\partial\bar{u}}{\partial t} = -\frac{\pi^2}{4}\frac{\bar{u}}{\eta^2} + \frac{\pi^2}{12}\,We\,\frac{\partial^3\eta}{\partial x^3}, \tag{4}$$

which as well as the diffusive-like dynamics on large lateral scales, also supports decaying wavelike dynamics at finite lateral length scales.† Furthermore, models such as (2)–(3) resolve finer details in space than a lubrication model, see § 5, and resolve faster dynamics in time, see § 4, than do lubrication models such as (1).

† On a film of non-dimensional thickness 1, small perturbations in η and $\bar{u}$ proportional to $\exp(\mathrm{i}kx + \lambda t)$ of wavenumber k and governed by (4) have frequency $\mathrm{Im}\,\lambda \approx k^2\pi\sqrt{We/(12\,Re)}$, for lateral wavenumbers $k \gg 1/\sqrt[4]{Re\,We}$, while decaying with rate $\mathrm{Re}\,\lambda = -\pi^2/(8\,Re)$.

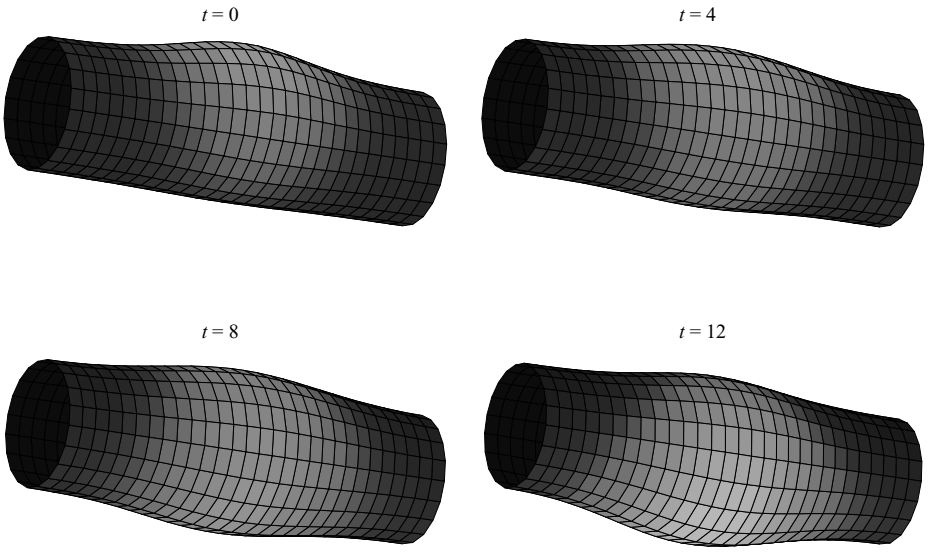

FIGURE 1. Around a nearly horizontal cylinder of radius $R = 2$ (not shown) we start with a fluid layer of thickness $\eta = 1$ except for a small bump discernible off the top dead centre of the cylinder. With Reynolds number $Re = 10$ in a vertical gravitational field, the fluid bump first slides around the cylinder to the bottom by non-dimensional time $t = 12$. The other sections of the fluid also slide down to the bottom of the cylinder, but not so fast.

Here, we greatly extend the model (2)–(3) by deriving in § 5 the approximate model for the flow of a three-dimensional thin liquid layer of an incompressible Newtonian fluid over an arbitrary solid, stationary and curved substrate, such as the flow about a cylinder shown in figures 1 and 2. The derived accurate model (57)–(58) for the film thickness η and an average lateral velocity $\bar{\boldsymbol{u}}$, defined in (47), encompasses many interactions between the various physical processes of fluid conservation, inertia, gravity, surface tension and substrate curvature. A simpler version of the model just describes the leading influences of these physical processes and is‡

$$\frac{\partial \eta}{\partial t} \approx -\nabla \cdot (\eta \bar{\boldsymbol{u}}), \tag{5}$$

$$Re\,\frac{\partial \bar{\boldsymbol{u}}}{\partial t} \approx -\left[\frac{\pi^2}{4}\frac{\bar{\boldsymbol{u}}}{\eta^2} + (2\boldsymbol{K} + \kappa \boldsymbol{I}) \cdot \frac{\bar{\boldsymbol{u}}}{\eta}\right] + \frac{\pi^2}{12}(We\,\nabla\tilde{\kappa} + Gr\,\boldsymbol{g}_s), \tag{6}$$

where $Gr\,\boldsymbol{g}_s$ is the component of gravity tangential to the substrate. The conservation of fluid equation (5) naturally generalizes equation (2) to three-dimensional flow. The momentum equation (6) similarly generalizes (3) to three-dimensional flow through a non-trivial effect of substrate curvature upon the drag. The important feature of this model, as in (2)–(3), is the incorporation of the dynamics of the inertia of the fluid, represented here by the leading-order term $Re\,\partial\bar{\boldsymbol{u}}/\partial t$, which enables the model to resolve wavelike behaviour. In contrast, the lubrication model of thin films (1) only encompasses a much more restricted range of dynamics. Many models have previously been derived to incorporate inertia, although mostly only for two-dimensional flow, for example, Shkadov (1967) integrated across the fluid film the approximate

‡ The approximate equality in the conservation of mass equation (5) becomes exact equality when ζ replaces η on the left-hand side. The higher-order analysis leading to (57) does this automatically.

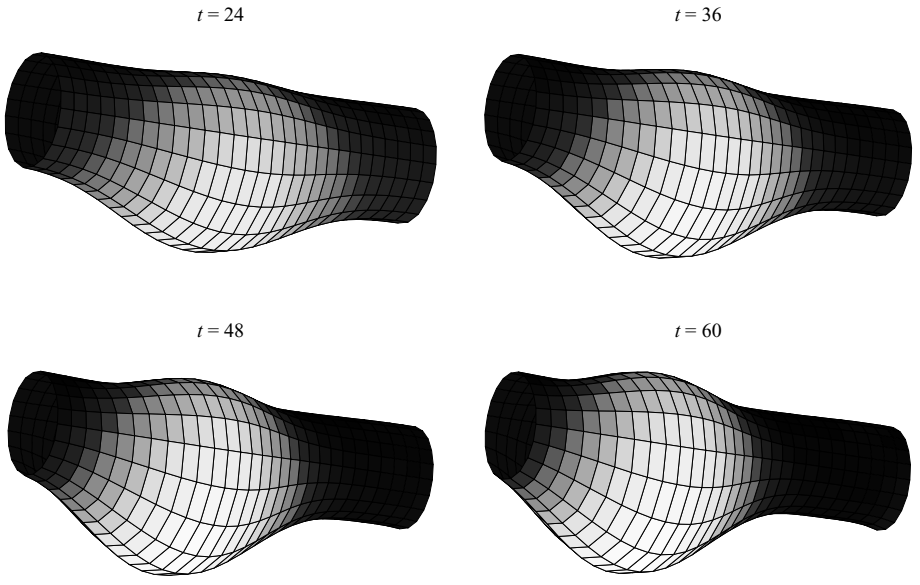

FIGURE 2. Around the nearly horizontal cylinder of radius $R = 2$ (not shown but at angle 0.1 radians to the horizontal) the fluid lump now, $t = 24$, at the bottom of the cylinder slowly pulls in fluid from the two ends of the cylinder under surface tension. By non-dimensional times $t = 48$ and 60, surface tension forms a large off-centre bead which slowly slides along the cylinder, surrounded by a thin layer, $\eta \approx 0.1$, still covering the cylinder.

boundary-layer equations to produce the widely used IBL model for two-dimensional flow on a flat plate (see Chang 1994, p. 110); Nguyen & Balakotaiah (2000) and Ruschak & Weinstein (2003) developed a model for the steady two-dimensional flow over a curved substrate based on assuming a cubic cross-film velocity structure; Ruyer-Quil & Manneville (2000) and Chang *et al.* (2002) use a small number of Galerkin modes for the cross-film structure to model the flow down an inclined flat plate; and Khayat, Kim & Delosquer (2004) implement a spectral numerical method to simulate axisymmetric flows on an axisymmetric substrate. Instead, we base the derivation of the model (5)–(6) on the approach established in § 4 that is supported by centre manifold theory. The approach is founded on viscosity damping all the lateral shear modes of the thin fluid film except the shear mode of slowest decay. Then *all* the physical interactions between spatial varying quantities, substrate curvature, surface tension and gravitational forcing, as seen in the particular simulation shown in figures 1 and 2, are systematically incorporated into the modelling, to some controlled order of error, because the centre manifold is made up of the slowly evolving solutions of the Navier–Stokes and continuity equations, see the discussion in § 4.† For example, the $\pi^2/12$ coefficient in the momentum equations of models (3) and (6) is not 1: the coefficient of these terms would be 1 in modelling based upon the heuristic of cross-sectional averaging as in the IBL (e.g. Chang 1994, p. 110); but $\pi^2/12 = 0.8224$ is correct because it must be 1/3 of the viscous decay rate $\pi^2/4$ in order to match the leading 1/3 coefficient in the lubrication model (1). In our approach, the model is based upon actual solutions of the Navier–Stokes equations and so obtains all coefficients correctly.

† Although our models are expressed in terms of cross-film averaged lateral velocities, our methodology does not average the equations. The lateral velocity averages are merely useful parameters to characterize the local fluid flow.

To begin, and following Roy *et al.* (2002), we introduce in § 2 an orthogonal curvilinear coordinate system fitted to the substrate. The analysis then starts from the incompressible Navier–Stokes equations and boundary conditions recorded in § 3 for this special coordinate system. Thus, we derive the model for general smoothly curving substrates.

The derived model (57)–(58) reduces to a model for three-dimensional fluid flow on flat substrates upon setting the principal curvatures of the substrate, k_1 and k_2, equal to zero. For example, on a flat substrate, the simpler model (6) becomes

$$Re\,\frac{\partial \bar{\boldsymbol{u}}}{\partial t} \approx -\frac{\pi^2}{4}\frac{\bar{\boldsymbol{u}}}{\eta^2} + \frac{\pi^2}{12}(We\,\nabla^3\eta + Gr\,\boldsymbol{g}_s). \tag{7}$$

The higher-order accurate version of this model, recorded in § 6.1 as (64)–(66), extends to three-dimensional fluid flows the models for two-dimensional flows on flat substrates derived by Roberts (1998). In § 6.1, we report on the linearized dynamics, $\eta = 1 + h$ where both h and $\bar{\boldsymbol{u}}$ are small. One result is that

$$Re\,\bar{\omega}_t = -\frac{\pi^2}{4}\bar{\omega} + \nabla^2\bar{\omega}, \tag{8}$$

where $\bar{\omega} = \bar{v}_x - \bar{u}_y$ is a measure of the mean vorticity normal to the substrate in the flow of the film. Thus, we predict that mean normal vorticity just dissipates owing to drag ($-\bar{\omega}\pi^2/4$) and diffusion ($\nabla^2\bar{\omega}$). However, letting $\bar{\delta} = \bar{u}_x + \bar{v}_y$, which measures the mean divergence of the flow of the fluid and hence indicates whether the film is thinning or thickening, we find

$$h_t = -\bar{\delta}, \tag{9}$$

$$Re\,\bar{\delta}_t = -\frac{\pi^2}{4}\bar{\delta} + \frac{\pi^2}{12}[Gr\,g_n\nabla^2 h + We\,\nabla^4 h] + 4.0930\,\nabla^2\bar{\delta}. \tag{10}$$

Observe that this divergence $\bar{\delta}$ diffuses with a larger coefficient, namely 4.093, than that of pure molecular diffusion; this effect is analogous to the enhanced Trouton viscosity of deforming viscous sheets (e.g. Ribe 2001, p. 143). The enhanced viscous dissipation is due to interactions with the shear flow similar to those giving rise to enhanced dispersion of a passive tracer in pipes (e.g. Mercer & Roberts 1994). From (10) observe that the divergence of the film's velocity is simply driven by gravity and surface tension acting on variations of the film's thickness and is dissipated by substrate drag and the enhanced lateral diffusion. Nonlinearities and substrate curvature modify this simple picture of the dynamics.

Circular cylinders are a specific substrate of wide interest. For example, Jensen (1997) studied the effects of surface tension on a thin liquid layer lining the interior of a cylindrical tube and derived a corresponding evolution equation; Alekseenko *et al.* (1996) studied evolution of rivulet flow underneath a sloping cylinder; Atherton & Homsy (1976), Kalliadasis & Chang (1994) and Kliakhandler, Davis & Bankoff (2001) considered coating flow down vertical fibres and gave nonlinear lubrication models for axisymmetric slow flow. Thus, in § 6.2, we also record the accurate model for flow both inside and outside a cylinder as used in the simulation for figures 1 and 2.

Axisymmetric flows are often of interest in coating flows. Using s as the axial coordinate, a basic model for axisymmetric fluid film flow along a cylinder of radius R is

$$\frac{\partial}{\partial t}\left(\eta \pm \frac{\eta^2}{2R}\right) = -\frac{\partial(\eta\bar{u})}{\partial s}, \tag{11}$$

$$Re\,\frac{\partial \bar{u}}{\partial t} \approx -\frac{\pi^2}{4}\frac{\bar{u}}{\eta^2} \pm \frac{\bar{u}}{R\eta} - 0.6487\frac{\bar{u}}{R^2} + \frac{\pi^2}{12}\,We\left(\frac{1}{R^2}\frac{\partial \eta}{\partial s} + \frac{\partial^3 \eta}{\partial s^3}\right) + Gr\left(\frac{\pi^2}{12}g_s \pm 0.4891\frac{g_s\eta}{R}\right), \tag{12}$$

where the upper/lower sign corresponds to flow on the outside/inside surfaces of the cylinder. Observe that the curvature of the substrate: in (11) modifies the expression of conservation of mass; drives a beading effect through η_s/R^2 in (12); and modifies the drag terms in (12). These are just some special cases of the models on different substrates which are recorded in detail in § 6.

The centre manifold approach we use to derive low-dimensional dynamical models such as (5)–(6) has many advantages: as discussed in detail in § 4, theory supports the existence, flexible construction and, importantly, the relevance of the modelling. Moreover, the approach leads to straightforward algebraic techniques for the derivation of the low-dimensional models (Roberts 1997), and to the correct modelling of initial conditions (Roberts 1989; Cox & Roberts 1995; Suslov & Roberts 1998) and boundary conditions (Roberts 1992). However, herein we limit attention to deriving the basic differential equations of the dynamical flow of the fluid. Other aspects of modelling remain for further study. At the end of § 5, we investigate high-order refinements of the basic linearized surface-tension-driven dynamics of (8)–(10) and determine that the model (57)–(58) derived here requires that spatial gradients are significantly less than the limit $|\nabla\eta| < 1.9$, see (62). This is the first time such a good estimate of the limit of applicability of inertia resolving models for fluid flow has been obtained. This quantitative indication of the extent of the model's spatial resolution is significantly better than that for lubrication models such as (1) which require the surface slope to be significantly less than 0.74 instead. Such quantitative estimates of the range of applicability are found through the systematic nature of the centre manifold approach to modelling.

2. The orthogonal curvilinear coordinate system

In this section we describe the general differential geometry necessary to consider flows in general non-Cartesian orthogonal coordinate system adapted to the curving substrate. Following Roy *et al.* (2002), we introduce the geometry of the substrate, then extend a coordinate out into space and establish the orthogonal curvilinear coordinate system used to describe the fluid flow.

Let $\mathscr{S}$ denote the solid substrate. When $\mathscr{S}$ has no umbilical point, that is, there is no point on $\mathscr{S}$ at which the two principal curvatures coincide, then there are exactly two mutually orthogonal principal directions in the tangent plane at every point in $\mathscr{S}$ (Guggenheimer 1963, Theorem 10-3). Let $\boldsymbol{e}_1$ and $\boldsymbol{e}_2$ be the unit vectors in these principal directions, and let $\boldsymbol{e}_3$ be the unit normal to the substrate to the side of the fluid so that $\boldsymbol{e}_1$, $\boldsymbol{e}_2$ and $\boldsymbol{e}_3$ form a right-handed curvilinear orthonormal set of unit vectors. Such a coordinate system is called a Darboux frame (Guggenheimer 1963). Let x_1 and x_2 be two parameters such that the unit tangent vector of a parameter curve $x_2 =$ constant is $\boldsymbol{e}_1$, the unit tangent vector of a parameter curve $x_1 =$ constant is $\boldsymbol{e}_2$, and let y measure the normal distance from the substrate. Then on the substrate, points $\boldsymbol{P} \in \mathscr{S}$,

$$\boldsymbol{e}_i = \frac{1}{m_i}\frac{\partial \boldsymbol{P}}{\partial x_i}, \tag{13}$$

for subscript $i = 1, 2$ here and later, with substrate scale factor

$$m_i = \left| \frac{\partial \boldsymbol{P}}{\partial x_i} \right|. \tag{14}$$

Further, the unit normal varies along the substrate with

$$\frac{\partial \boldsymbol{e}_3}{\partial x_i} = -m_i k_i \boldsymbol{e}_i, \tag{15}$$

where k_i are the corresponding principal curvatures of the substrate. The unit vectors $\boldsymbol{e}_i$ are independent of the normal coordinate y. At any point in the fluid, written as

$$\boldsymbol{X}(x_1, x_2, y) = \boldsymbol{P}(x_1, x_2) + y\boldsymbol{e}_3(x_1, x_2),$$

the scale factors of the spatial coordinate system are, since positive curvature corresponds to a concave coordinate curve,

$$h_i = \left| \frac{\partial \boldsymbol{X}}{\partial x_i} \right| = m_i(1 - k_i y), \quad h_3 = \left| \frac{\partial \boldsymbol{X}}{\partial y} \right| = 1.$$

The spatial derivatives of the curvilinear unit vectors are (Batchelor 1979, p. 598)

$$\frac{\partial \boldsymbol{e}_i}{\partial x_i} = -\frac{h_{i,i'}}{h_{i'}} \boldsymbol{e}_{i'} + m_i k_i \boldsymbol{e}_3, \qquad \frac{\partial \boldsymbol{e}_i}{\partial y} = \frac{\partial \boldsymbol{e}_3}{\partial y} = \boldsymbol{0},$$
$$\frac{\partial \boldsymbol{e}_3}{\partial x_i} = -m_i k_i \boldsymbol{e}_i, \qquad \frac{\partial \boldsymbol{e}_i}{\partial x_{i'}} = \frac{h_{i',i}}{h_i} \boldsymbol{e}_{i'}.$$

where $i' = 3 - i$ is the complementary index of i, $h_{i,j}$ denotes $\partial h_i / \partial x_j$, and repeated subscripts i or i' do not denote summation.

A fundamental geometric quantity is the free-surface mean curvature $\tilde{\kappa}$ which is involved in the effects of surface tension through the energy stored in the free surface. As derived by Roy *et al.* (2002), see their equation (37), the mean curvature of the free surface

$$\tilde{\kappa} = \frac{1}{\tilde{h}_1 \tilde{h}_2} \left[\frac{\partial}{\partial x_1} \left(\frac{\tilde{h}_2^2 \eta_{x_1}}{\mathscr{A}} \right) + \frac{\partial}{\partial x_2} \left(\frac{\tilde{h}_1^2 \eta_{x_2}}{\mathscr{A}} \right) \right] + \frac{1}{\mathscr{A}} \left[(\tilde{h}_1^2 + \eta_{x_1}^2) \frac{m_2 k_2}{\tilde{h}_1} + (\tilde{h}_2^2 + \eta_{x_2}^2) \frac{m_1 k_1}{\tilde{h}_2} \right],$$

where $\tilde{h}_i = m_i(1 - k_i \eta)$ are the metric coefficients evaluated on the free surface (as generally indicated by the tilde), and where

$$\mathscr{A} = \sqrt{\tilde{h}_1^2 \tilde{h}_2^2 + \tilde{h}_2^2 \eta_{x_1}^2 + \tilde{h}_1^2 \eta_{x_2}^2},$$

is proportional to the free-surface area above a patch $dx_1 \times dx_2$ of the curving substrate.

We assume the film of fluid is thin. However, we adopt a non-dimensionalization based on the thickness of the fluid film. Thus, on the scale of the fluid thickness, the viscous fluid is of large horizontal extent on a slowly curving substrate. Consequently, we treat as small the lateral spatial derivatives of the fluid flow and the curvatures of the substrate; Decré & Baret (2003, p. 162) report experiments showing that even apparently rapid changes in the substrate may be treated as slow variations in the mathematical model. Then, an approximation to the curvature of the free surface is

$$\tilde{\kappa} = \nabla^2 \eta + \frac{k_1}{1 - k_1 \eta} + \frac{k_2}{1 - k_2 \eta} + O(\kappa^3 + \nabla^3 \eta), \tag{16}$$

where in the substrate coordinate system the Laplacian

$$\nabla^2\eta = \frac{1}{m_1 m_2}\left[\frac{\partial}{\partial x_1}\left(\frac{m_2}{m_1}\frac{\partial \eta}{\partial x_1}\right) + \frac{\partial}{\partial x_2}\left(\frac{m_1}{m_2}\frac{\partial \eta}{\partial x_2}\right)\right]. \tag{17}$$

For later use, also observe that on the free surface, two unit tangent vectors $\tilde{\boldsymbol{t}}_i$ and unit normal vector $\tilde{\boldsymbol{n}}$ are

$$\tilde{\boldsymbol{t}}_i = (\tilde{h}_i \boldsymbol{e}_1 + \eta_{x_i}\boldsymbol{e}_3)/\sqrt{\tilde{h}_i^2 + \eta_{x_i}^2}, \tag{18}$$

$$\tilde{\boldsymbol{n}} = (-\tilde{h}_2\eta_{x_1}\boldsymbol{e}_1 - \tilde{h}_1\eta_{x_2}\boldsymbol{e}_2 + \tilde{h}_1\tilde{h}_2\boldsymbol{e}_3)/\mathscr{A}. \tag{19}$$

We describe the dynamics of the fluid using these formulae in a coordinate system determined by the substrate upon which the fluid film flows.

3. Equations of motion and boundary conditions

Having developed the intrinsic geometry of general three-dimensional surfaces, we proceed to record the Navier–Stokes equations and boundary conditions for a Newtonian fluid in this curvilinear coordinate system.

Consider the Navier–Stokes equations for an incompressible fluid moving with velocity field $\boldsymbol{u}$ and with pressure field p. The flow dynamics are driven by pressure gradients along the substrate which are caused by both surface-tension forces, coefficient σ (the forces varying owing to variations of the curvature of the free surface of the fluid), and an acceleration due to gravity, $\boldsymbol{g}$, of magnitude g in the direction of the unit vector $\hat{\boldsymbol{g}}$. Then the continuity and Navier–Stokes equations are

$$\nabla\cdot\boldsymbol{u} = 0, \tag{20}$$

$$\frac{\partial \boldsymbol{u}}{\partial t} + \boldsymbol{u}\cdot\nabla\boldsymbol{u} = -\frac{1}{\rho}\nabla p + \frac{\mu}{\rho}\nabla^2\boldsymbol{u} + \boldsymbol{g}. \tag{21}$$

We adopt a non-dimensionalization based on the characteristic thickness of the film H, and some characteristic lateral velocity U: for a specific example, in a regime where surface tension drives a flow against viscous drag, the characteristic velocity $U = \sigma/\mu$, and the Weber number then becomes $We = \sigma/(U\mu) = 1$. Reverting to the general case, the reference length is H, the reference time H/U, and the reference pressure $\mu U/H$. Then the non-dimensional fluid equations are

$$\nabla\cdot\boldsymbol{u} = 0, \tag{22}$$

$$Re\left[\frac{\partial \boldsymbol{u}}{\partial t} + \boldsymbol{u}\cdot\nabla\boldsymbol{u}\right] = -\nabla p + \nabla^2\boldsymbol{u} + Gr\,\hat{\boldsymbol{g}}, \tag{23}$$

where $Re = UH\rho/\mu$ is a Reynolds number characterizing the importance of the inertial terms compared to viscous dissipation, and $Gr = g\rho H^2/(\mu U)$ is a gravity number analogously measuring the importance of the gravitational body force compared to viscous dissipation; the gravity number $Gr = Re\,/\,Fr$ for Froude number $Fr = U^2/gH$ so that when the reference velocity is chosen to be the inviscid shallow-water wave speed $U = \sqrt{gH}$, then $Fr = 1$ and the gravity number $Gr = Re$.

In the curvilinear coordinate system defined in § 2, the non-dimensional continuity and Navier–Stokes equations for the velocity field $\boldsymbol{u} = u_1\boldsymbol{e}_1 + u_2\boldsymbol{e}_2 + v\boldsymbol{e}_3$ are (adapted from Batchelor 1979, p. 600):

$$\frac{\partial}{\partial x_1}(h_2u_1) + \frac{\partial}{\partial x_2}(h_1u_2) + \frac{\partial}{\partial y}(h_1h_2v) = 0, \tag{24}$$

$$Re\left\{\frac{\partial \boldsymbol{u}}{\partial t}+\boldsymbol{e}_1\left[\boldsymbol{u}\cdot\nabla u_1+\frac{u_2}{h_1h_2}\left(u_1\frac{\partial h_1}{\partial x_2}-u_2\frac{\partial h_2}{\partial x_1}\right)-m_1k_1\frac{vu_1}{h_1}\right]\right.$$
$$+\boldsymbol{e}_2\left[\boldsymbol{u}\cdot\nabla u_2+\frac{u_1}{h_1h_2}\left(u_2\frac{\partial h_2}{\partial x_1}-u_1\frac{\partial h_1}{\partial x_2}\right)-m_2k_2\frac{vu_2}{h_2}\right]$$
$$\left.+\boldsymbol{e}_3\left[\boldsymbol{u}\cdot\nabla v+m_1k_1\frac{{u_1}^2}{h_1}+m_2k_2\frac{{u_2}^2}{h_2}\right]\right\}=-\nabla p-\nabla\times\boldsymbol{\omega}+Gr\,\hat{\boldsymbol{g}}, \tag{25}$$

where $\boldsymbol{\omega}$ is the vorticity of the fluid given by the curl

$$\boldsymbol{\omega}=\nabla\times\boldsymbol{u}=\frac{\boldsymbol{e}_1}{h_2}\left[\frac{\partial v}{\partial x_2}-\frac{\partial(h_2u_2)}{\partial y}\right]+\frac{\boldsymbol{e}_2}{h_1}\left[\frac{\partial(h_1u_1)}{\partial y}-\frac{\partial v}{\partial x_1}\right]$$
$$+\frac{\boldsymbol{e}_3}{h_1h_2}\left[\frac{\partial(h_2u_2)}{\partial x_1}-\frac{\partial(h_1u_1)}{\partial x_2}\right],$$

and where

$$\boldsymbol{u}\cdot\nabla=\frac{u_1}{h_1}\frac{\partial}{\partial x_1}+\frac{u_2}{h_2}\frac{\partial}{\partial x_2}+v\frac{\partial}{\partial y}.$$

We solve these partial differential equations with the following boundary conditions.

(i) The fluid does not slip along the stationary substrate $\mathscr{S}$:

$$\boldsymbol{u}=\boldsymbol{0}\quad\text{on } y=0. \tag{26}$$

(ii) The fluid satisfies the free-surface kinematic boundary condition

$$\frac{\partial\eta}{\partial t}=v-\frac{u_1}{\tilde{h}_1}\frac{\partial\eta}{\partial x_1}-\frac{u_2}{\tilde{h}_2}\frac{\partial\eta}{\partial x_2}\quad\text{on } y=\eta. \tag{27}$$

(iii) Surface tension causes the normal surface stress to be, in non-dimensional form,

$$\tilde{\boldsymbol{n}}\cdot\tilde{\boldsymbol{\tau}}\cdot\tilde{\boldsymbol{n}}=\tilde{p}+We\,\tilde{\kappa}, \tag{28}$$

where $\tilde{\boldsymbol{\tau}}$ is the deviatoric stress tensor on free surface, $\tilde{p}$ is the fluid pressure at the surface relative to the assumed zero pressure of the negligible medium above the fluid, and $\tilde{\boldsymbol{n}}$ is the unit normal to the free surface.

(iv) The free surface has zero tangential stress

$$\tilde{\boldsymbol{t}}\cdot\tilde{\boldsymbol{\tau}}\cdot\tilde{\boldsymbol{n}}=0, \tag{29}$$

where $\tilde{\boldsymbol{t}}$ is any tangent vector to the free surface. We use the two linearly independent tangent vectors in (18) to ensure the boundary condition is satisfied for all tangent vectors.

In this curvilinear coordinate system the components of the non-dimensional deviatoric stress tensor $\boldsymbol{\tau}$ are (Batchelor 1979, p. 599)

$$\left.\begin{aligned}
\tau_{ii}&=2\left(\frac{1}{h_i}\frac{\partial u_i}{\partial x_i}+\frac{h_{i,i'}}{h_ih_{i'}}u_{i'}-\frac{m_ik_i}{h_i}v\right),\\
\tau_{12}&=\frac{1}{h_2}\frac{\partial u_1}{\partial x_2}+\frac{1}{h_1}\frac{\partial u_2}{\partial x_1}-\frac{h_{1,2}}{h_1h_2}u_1-\frac{h_{2,1}}{h_1h_2}u_2,\\
\tau_{i3}&=\frac{1}{h_i}\frac{\partial v}{\partial x_i}+\frac{\partial u_i}{\partial y}+\frac{m_ik_i}{h_i}u_i,\\
\tau_{33}&=2\frac{\partial v}{\partial y}.
\end{aligned}\right\} \tag{30}$$

4. Centre manifold theory supports the model

We adapt the governing fluid equations (24)–(25) and the four boundary conditions (26)–(29) to a form suitable for the application of centre manifold theory and techniques to provide the low-dimensional dynamical model with firm theoretical support.

First, summarize centre manifold theory to clarify the support it gives to modelling fluid dynamics. See, for example, Carr (1981), Iooss & Peroueme (1993) and Kuznetsov (1995) for more details. Consider a dynamical system for the evolution of the physical variables $\boldsymbol{v}(t)$ (such as fluid velocity) in the form

$$\frac{\partial \boldsymbol{v}}{\partial t} = \mathscr{L}\boldsymbol{v} + \boldsymbol{f}(\boldsymbol{v}, \boldsymbol{\epsilon}), \tag{31}$$

where $\mathscr{L}$ is a linear operator (such as cross-film diffusion), $\boldsymbol{f}$ is a smooth nonlinear function of $\boldsymbol{v}$ and $\boldsymbol{\epsilon}$ (such as advection of momentum) and $\boldsymbol{\epsilon}$ is a vector of parameters (such as the magnitude of lateral slowly varying gradients, and the gravitational forcing Gr). The precondition for the theory is that the linear operator has some eigenvalues λ, say n of them, with zero real part (such as those associated with conservation principles) and the remaining eigenvalues have strictly negative real parts, $\operatorname{Re}\lambda < -\alpha < 0$ (such as those of viscous damping). The theory asserts that the n modes corresponding to the eigenvalues of zero real part can be used to describe the long-term evolution from quite general initial conditions: thus, let the n-dimensional vector $\boldsymbol{a}$, say, measure the amplitude (such as the fluid thickness and the mean lateral velocities) of the n critical modes. Then three crucial theorems follow *in some finite size neighbourhood of the origin in* $(\boldsymbol{v}, \boldsymbol{\epsilon})$*-space*. Here, the 'finite size neighbourhood' are those slow flows where the lateral derivatives are small enough; for example, analysis leading to the upper bound (62) suggests one bound on the size of the neighbourhood is that gradients of the fluid thickness must satisfy $|\nabla\eta| < 1.9$. The following theorems hold for this neighbourhood of the origin.

Existence. Solutions exist to the physical equations (31) parameterized by evolving amplitudes $\boldsymbol{a}(t)$ and constant parameters $\boldsymbol{\epsilon}$:

$$\boldsymbol{v} = \boldsymbol{V}(\boldsymbol{a}, \boldsymbol{\epsilon}) \quad \text{such that} \quad \frac{\partial \boldsymbol{a}}{\partial t} = \boldsymbol{G}(\boldsymbol{a}, \boldsymbol{\epsilon}), \tag{32}$$

for some smooth functions $\boldsymbol{V}$ and $\boldsymbol{G}$; the hypersurface $\boldsymbol{v} = \boldsymbol{V}(\boldsymbol{a}, \boldsymbol{\epsilon})$ is called the centre manifold. In applications, $\partial \boldsymbol{a}/\partial t = \boldsymbol{G}$ forms the model, such as (2)–(3), whereas $\boldsymbol{V}$ describes the physical fields such as those we see later in (50)–(52).

The model (32) describes only a subset of the possible solutions of the full physical problem (31), namely that subset lying within the centre manifold. In our application to fluid film dynamics, the subset of flows described by the model are those with relatively simple cross-film shear structure (for example, see the cross-film structure functions plotted in figure 4). Modes with convoluted cross-film shear flow are rapidly damped by viscosity and lead to the following relevance theorem.

Relevance. *All* solutions of the physical problem (31) are attracted exponentially quickly in time to solutions of the model (32). Express this more rigorously as: for all solutions $\boldsymbol{v}(t)$ of (31) which stay in the neighbourhood, there exists a solution $\boldsymbol{a}(t)$ of the model (32) such that $\|\boldsymbol{v}(t) - \boldsymbol{V}(\boldsymbol{a}(t), \boldsymbol{\epsilon})\| = O(\exp(-\alpha t))$ for some upper bound $-\alpha$ on the negative eigenvalues of the linear operator $\mathscr{L}$.

This property is immensely important as it asserts the model is faithful to the physical dynamics. Most other modelling methodologies either appeal only to some asymptotic self-consistency, such as the method of multiple scales, or to a shadowing

property (there is a nearby system that the model follows). However, centre manifold theory assures us that once initial transients have decayed in time, the original system does follow the model. Furthermore, this assurance applies in some finite domain (the neighbourhood), the assurance is not just asymptotic.

Approximation. The limitation is that we can only construct the centre manifold model (32) approximately, usually as an asymptotic expansion in the amplitudes $\boldsymbol{a}$ and parameters $\boldsymbol{\epsilon}$. However, the approximation theorem asserts that substituting (32) into the physical system (31) and hence solving

$$\frac{\partial \boldsymbol{v}}{\partial t} = \frac{\partial \boldsymbol{V}}{\partial \boldsymbol{a}}\boldsymbol{G} = \mathscr{L}\boldsymbol{V} + \boldsymbol{f}(\boldsymbol{V}, \boldsymbol{\epsilon}) \tag{33}$$

to some order of error in $(\boldsymbol{a}, \boldsymbol{\epsilon})$ results in the model (32) being correct to the same order of error. That is, *the order of error of the model is the same as the order of residuals of the physical equations.*

This property also has immense repercussions in application as it empowers us with enormous flexibility in truncating asymptotic approximations to the model. Thus, as we use here, we justify creating models resolving many and varied physical effects which in different situations, or even on different parts of the substrate, have different physical balances. Moreover, the centre manifold model need not be constructed within the straight jacket of one scenario of relative magnitudes of the physical parameters, but can, as here, be constructed quite generally for later truncation in any given circumstance as required by the particular application. The approximation theorem asserts that such flexible truncations form consistent models.

Three mathematical artifices place the equations within the centre manifold framework; these artifices fit the parameter regime of viscous flow varying relatively slowly over a substrate.

(i) We introduce the small parameter ϵ to characterize both the small lateral gradients along the substrate, $\partial/\partial x_i$, and the small curvatures of the substrate (as curvatures are also lateral gradients, namely the partial derivatives of the unit normal with respect to x_i). The parameter ϵ may be viewed either as a mathematical artifice that simply counts the number of lateral derivatives in a term, or as being equivalent to the multiple-scale assumption of variations occurring only on a large lateral length scale (large compared to the thickness of the fluid).† The two viewpoints provide exactly the same results. In either case, let the lateral variations scale with the parameter ϵ:

$$\frac{\partial}{\partial x_i} = \epsilon \frac{\partial}{\partial x_i^*}, \quad k_1 = \epsilon k_1^*, \quad k_2 = \epsilon k_2^*, \quad \kappa = \epsilon \kappa^*,$$

where $*$ denotes quantities which have been scaled by ϵ.

(ii) The presumed small gravitational forcing is treated as a perturbing effect by expressing the model in a series in powers of the gravity number Gr.

(iii) We base the analysis on a problem where the mean lateral velocity becomes a natural amplitude (sometimes called an 'order parameter'). As introduced by Roberts (1998), the convenient way we choose to do this is to artificially force the lateral flow at the free surface, then remove the forcing to recover a model for the physical

† Basing the analysis upon long-wave asymptotics implies the model will not necessarily resolve the finite wavenumber (Tollmien–Schlichting) instabilities of the shear flow that Floryan, Davis & Kelly (1987) and Burya & Shkadov (2001) identify as the dominant instability on a nearly horizontal substrate. However, on a curved substrate, we expect long-wavelength dynamics generally to dominate as only limited parts of the substrate will be nearly horizontal.

fluid flow. Thus, we modify the tangential stress condition (29) on the free surface, to become (39), using a parameter γ: at $\gamma = 0$, the lateral shear mode of slowest decay becomes a marginally stable mode; whereas at $\gamma = 1$, the modification vanishes to restore the physical stress-free boundary condition (29). The modification to arrive at (39) is necessary to create the necessary three modes of the centre manifold model. Subsequently, evaluating at $\gamma = 1$ removes the modification to obtain a model for the physically correct dynamics. We present evidence in § 5 that the evaluation of the model at $\gamma = 1$ is sound.

Such modification, in conjunction with the centre manifold approach elaborated upon later in this section, is a very powerful tool for rational modelling of complicated physical processes; for example, similar modifications of the free-surface conditions enabled the large-scale modelling of turbulent floods by Mei, Roberts & Li (2003) based upon the k–ϵ turbulence closure. Such modification could also be employed in conjunction with other asymptotic modelling methods, such as the method of multiple scales.

(iv) Note: we do not rescale the velocity and pressure fields. In the centre manifold approach, the scalings for the physical fields follow in the solution of the fluid equations within the slowly varying assumption. For example, we later derive the pressure field (50) which shows $p = O(\epsilon\kappa + \epsilon^2 + \epsilon|\bar{\boldsymbol{u}}| + Gr)$ as a consequence of only the assumptions (i)–(iii) above. Our model of the pressure field is valid no matter which is the dominant physical influence, be it substrate curvature, free-surface curvature, gradients of velocity, or gravitational forcing, respectively seen in this order of magnitude. This is essential here where, for example, the substrate curvature may dominate in one locale, but not others. In the presence of complicated interactions between varied physical mechanisms, as we encompass here, we derive expressions for the physical fields that are valid over a wide range of different conventional scalings. *We need not assume a scaling for the unknown fields at the time of derivation – this is a major advantage of the centre manifold approach that follows from the approximation theorem.* Instead, we just require that the rates of specified physical processes are in some sense 'small' compared to the viscous decay of cross-film shear. We place no restriction nor relation on the relative magnitude of the various 'small' effects. The approximation theorem assures us that the errors in the model are of the same order in these 'small' effects as the residuals of the governing fluid equations.

Now rewrite the governing fluid equations according to the above three artifices so that we may apply centre manifold theory. The following fluid equations (34)–(40) correspond to equation (31) in the previous discussion of centre manifold theory: for example, if the introduced parameters ϵ and γ are set to one, then we recover precisely the physical Navier–Stokes equations and boundary conditions of § 3. For convenience, we drop the '$*$' superscript on all re-scaled variables hereinafter. Equations (24)–(25) become

$$\epsilon\frac{\partial}{\partial x_1}(h_2u_1) + \epsilon\frac{\partial}{\partial x_2}(h_1u_2) + \frac{\partial}{\partial y}(h_1h_2v) = 0, \tag{34}$$

$$\begin{aligned} Re\Bigg\{ \frac{\partial \boldsymbol{u}}{\partial t} + \boldsymbol{e}_1 \Bigg[&\epsilon\frac{u_1}{h_1}\frac{\partial u_1}{\partial x_1} + \epsilon\frac{u_2}{h_2}\frac{\partial u_1}{\partial x_2} + v\frac{\partial u_1}{\partial y} + \epsilon\frac{u_2}{h_1h_2}\left(u_1\frac{\partial h_1}{\partial x_2} - u_2\frac{\partial h_2}{\partial x_1}\right) \\ &- \epsilon m_1k_1\frac{vu_1}{h_1}\Bigg] + \boldsymbol{e}_2\Bigg[\epsilon\frac{u_1}{h_1}\frac{\partial u_2}{\partial x_1} + \epsilon\frac{u_2}{h_2}\frac{\partial u_2}{\partial x_2} + v\frac{\partial u_2}{\partial y} \\ &+ \epsilon\frac{u_1}{h_1h_2}\left(u_2\frac{\partial h_2}{\partial x_1} - u_1\frac{\partial h_1}{\partial x_2}\right) - \epsilon m_2k_2\frac{vu_2}{h_2}\Bigg] \end{aligned}$$

$$+\boldsymbol{e}_3\left[\epsilon\frac{u_1}{h_1}\frac{\partial v}{\partial x_1}+\epsilon\frac{u_2}{h_2}\frac{\partial v}{\partial x_2}+v\frac{\partial v}{\partial y}+\epsilon m_1k_1\frac{u_1^2}{h_1}+\epsilon m_2k_2\frac{u_2^2}{h_2}\right]\Bigg\}$$
$$=-\epsilon\frac{\boldsymbol{e}_1}{h_1}\frac{\partial p}{\partial x_1}-\epsilon\frac{\boldsymbol{e}_2}{h_2}\frac{\partial p}{\partial x_2}-\boldsymbol{e}_3\frac{\partial p}{\partial y}+\frac{1}{h_2}\left[\epsilon\frac{\partial\omega_3}{\partial x_2}-\frac{\partial\omega_2}{\partial y}\right]\boldsymbol{e}_1$$
$$+\frac{1}{h_1}\left[\frac{\partial\omega_1}{\partial y}-\epsilon\frac{\partial\omega_3}{\partial x_1}\right]\boldsymbol{e}_2+\frac{\epsilon}{h_1h_2}\left[\frac{\partial\omega_2}{\partial x_1}-\frac{\partial\omega_1}{\partial x_2}\right]\boldsymbol{e}_3+Gr\,\hat{\boldsymbol{g}}, \tag{35}$$

where the scale factors are $h_i=m_i(1-\epsilon k_i y)$, and the components of the vorticity are (recall $i'=3-i$)

$$\omega_{i'}=\frac{(-1)^i}{h_i}\left[\epsilon\frac{\partial v}{\partial x_i}-\frac{\partial(h_iu_i)}{\partial y}\right],\quad \omega_3=\frac{\epsilon}{h_1h_2}\left[\frac{\partial(h_2u_2)}{\partial x_1}-\frac{\partial(h_1u_1)}{\partial x_2}\right].$$

The boundary conditions (26)–(29) on the bed and the free surface become

$$\boldsymbol{u}=\boldsymbol{0}\quad\text{on } y=0, \tag{36}$$
$$\frac{\partial\eta}{\partial t}=v-\epsilon\frac{u_1}{\tilde{h}_1}\frac{\partial\eta}{\partial x_1}-\epsilon\frac{u_2}{\tilde{h}_2}\frac{\partial\eta}{\partial x_2}\quad\text{on } y=\eta, \tag{37}$$
$$\tilde{\boldsymbol{n}}\cdot\tilde{\boldsymbol{\tau}}\cdot\tilde{\boldsymbol{n}}=\tilde{p}+We\,\tilde{\kappa}, \tag{38}$$
$$\tilde{\boldsymbol{t}}_i\cdot\tilde{\boldsymbol{\tau}}\cdot\tilde{\boldsymbol{n}}=(1-\gamma)\frac{m_im_1m_2u_i}{\eta l_il}\quad\text{on } y=\eta, \tag{39}$$

where

$$l_i=\sqrt{\tilde{h}_i^2+\epsilon^2\eta_{x_i}^2},\quad l=\sqrt{(\epsilon\tilde{h}_2\eta_{x_1})^2+(\epsilon\tilde{h}_1\eta_{x_2})^2+(\tilde{h}_1\tilde{h}_2)^2},$$

the unit tangent vectors

$$\tilde{\boldsymbol{t}}_i=(\tilde{h}_i\boldsymbol{e}_i+\epsilon\eta_{x_i}\boldsymbol{e}_3)/l_i,$$

and unit normal vector

$$\tilde{\boldsymbol{n}}=(-\epsilon\tilde{h}_2\eta_{x_1}\boldsymbol{e}_1-\epsilon\tilde{h}_1\eta_{x_2}\boldsymbol{e}_2+\tilde{h}_1\tilde{h}_2\boldsymbol{e}_3)/l.$$

The asymptotic expressions for the deviatoric stress $\tilde{\boldsymbol{\tau}}$ on the free surface are

$$\left.\begin{aligned}
\tilde{\tau}_{ii}&=2\epsilon\left(\frac{1}{m_1}\frac{\partial u_i}{\partial x_i}+\frac{h_{i,i'}}{m_im_i'}u_i-k_iv\right)+O(\epsilon^2),\\
\tilde{\tau}_{12}&=\epsilon\left(\frac{1}{m_2}\frac{\partial u_1}{\partial x_2}+\frac{1}{m_1}\frac{\partial u_2}{\partial x_1}-\frac{h_{1,2}}{m_1m_2}u_1-\frac{h_{2,1}}{m_1m_2}u_2\right)+O(\epsilon^2),\\
\tilde{\tau}_{i3}&=\frac{\partial u_i}{\partial y}+\epsilon\left(k_iu_i+\frac{1}{m_i}\frac{\partial v}{\partial x_i}\right)+O(\epsilon^2),\\
\tilde{\tau}_{33}&=2\frac{\partial v}{\partial y},
\end{aligned}\right\} \tag{40}$$

and the mean curvature of the free surface $\tilde{\kappa}$, expanded in powers of ϵ, is

$$\tilde{\kappa}=\epsilon\kappa+\epsilon^2[\nabla^2\eta-\kappa_2\eta]+O(\epsilon^3),$$

where $\nabla^2\eta$ is the same as that in (17) and $\kappa_2=k_1^2+k_2^2$.

The tangential stress boundary condition (39) is modified by the introduction of the artificial parameter γ. We recover the physically correct boundary condition when $\gamma=1$. However, when $\gamma=0$, the boundary condition (39) linearizes to

$$\frac{\partial u_i}{\partial y}=\frac{u_i}{\eta}\quad\text{on } y=\eta,$$

which leads to two neutral horizontal shear modes, $u_i \propto y$. The above equations generalize the physical equations by introducing the extra artificial parameters ϵ and γ. Then by adjoining the trivial equations

$$\frac{\partial \epsilon}{\partial t} = 0, \quad \frac{\partial \gamma}{\partial t} = 0, \quad \frac{\partial\, Gr}{\partial t} = 0, \tag{41}$$

we obtain a new but equivalent dynamical system in the variables $\boldsymbol{u}$, η, p, ϵ, γ and Gr. The original system will be recovered by setting $\epsilon = 1$ and $\gamma = 1$. However, the two systems are quite different with regard to center manifold theory. The theory now treats all terms that are multiplied by the three small parameters as 'nonlinear' perturbing effects on the system. So the dynamics we describe will be suitable only when there are slow lateral variations in x_i of the curvatures of the substrate, of $\boldsymbol{u}$, p and η, small ϵ, and a relatively weak gravitational forcing on the system, small Gr. In § 5, we argue that evaluating at $\gamma = 1$ is sound – that is, $\gamma = 1$ lies within the neighbourhood referred to in the theory – and towards the end of § 5 we give evidence that lateral variations are slow enough when the logarithmic derivative of the gradients are significantly less than $1.9/\eta$.

The linear dynamics are fundamental to the application of centre manifold techniques to derive a low-dimensional model. The linear part of system (34)–(39), that is, omitting the nonlinear advection and all terms multiplied by a small parameter ϵ, γ or Gr, is

$$\frac{\partial v}{\partial y} = 0, \tag{42}$$

$$Re\,\frac{\partial \boldsymbol{u}}{\partial t} + \boldsymbol{e}_3 \frac{\partial p}{\partial y} - \frac{\partial^2 \boldsymbol{u}}{\partial y^2} = 0, \tag{43}$$

with the boundary conditions (36)–(39) linearized to

$$\left.\begin{array}{ll} \boldsymbol{u} = \boldsymbol{0} & \text{on } y = 0, \\ \dfrac{\partial \eta}{\partial t} - v = 0 & \text{on } y = \eta, \\ 2\dfrac{\partial v}{\partial y} - p = 0 & \text{on } y = \eta, \\ \dfrac{\partial u_i}{\partial y} - \dfrac{u_i}{\eta} = 0 & \text{on } y = \eta. \end{array}\right\} \tag{44}$$

Note that there are no curvature nor lateral variations in the above linear equations as in the slowly varying approximation such variations do not affect the viscous decay of lateral shear that is the dominant linear process. The linear dynamical system has three types of solution:

(i) a motionless fluid film of constant thickness $u = v = p = 0$, $\eta = \text{constant}$;

(ii) the family of decaying lateral shear modes – the mode with non-dimensional cross-film wavenumber ℓ is $u_i \propto \sin(\ell y/\eta)\exp(\lambda t)$ where

$$\lambda = -\frac{\ell^2}{Re\,\eta^2}, \quad \text{such that} \quad \ell \cot \ell = 1; \tag{45}$$

(iii) the trivial parameters ϵ, γ and Gr being independently constant.

Thus, the six modes corresponding to zero eigenvalues, the so-called critical modes, are the four modes with η, ϵ, γ and Gr arbitrarily constant, and the two lateral shear modes with $u_i \propto y$ (obtained in the limit as the cross-film wavenumber $\ell \to 0$). All other modes have strictly negative eigenvalues from (45) and correspond to viscously

damped lateral shear modes. Consequently, the centre manifold model which we create has six modes: three corresponding to critical physical modes; and three corresponding to trivial parameter modes.

The above eigenanalysis applies independently at each lateral location $\boldsymbol{x}$ of the substrate. However, as argued by Roberts (1988), under the slowly varying assumption, we view each 'position' as a physical locale that is laterally much wider than the depth of the fluid, but much smaller than the lateral length scales of interest. Thus, the critical physical modes of the centre manifold arise independently at each locale (Roberts 1988), and so the centre manifold is parameterized by the amplitude of the critical modes at the 'infinite number' of locations on the substrate, that is, by the average lateral velocity $\bar{\boldsymbol{u}}(\boldsymbol{x}, t)$ and the fluid thickness $\eta(\boldsymbol{x}, t)$ at each $\boldsymbol{x}$. Then in the later fully nonlinear analysis, the lateral derivatives in the governing equations couple neighbouring locations together to obtain a model expressed in the classic form of a system of partial differential equations such as (5)–(6). In the slowly varying regime, this coupling is weak and the 'small' parameter ϵ systematically organizes the interactions for us in the full nonlinear analysis. In this manner, we base the 'infinite dimensional' centre manifold model upon the above cross-film dynamics.

Centre manifold techniques are justifiably applied to infinite dimensional dynamical systems with a separation of linear dynamics and such that the nonlinear perturbation terms in the system are smooth and bounded (Gallay's 1993, theorem 4.1) (alternatively see Chicone & Latushkin 1997). Here, the linear dynamics (42)–(44) have a well-structured centre space and stable space identified through the eigenvalues (45); the main novelty is that the cross-film dynamics apply at each position independently of each other and hence generate an 'infinite dimensional' centre manifold. However, here the perturbation terms in system (34)–(35), as they involve spatial derivatives, are unbounded so Gallay's (1993) prerequisite condition (A 2) is not satisfied; nonetheless, by restricting the Banach space to sufficiently slowly varying functions (Roberts 1988) the derivatives remain bounded and the theory then assures us that a centre manifold model exists. (Alternatively, we could replace all the lateral derivatives by bounded operators that match the physical derivatives for long waves, but which are bounded for high wavenumbers. Then centre manifold theory applies strictly and assures the existence of a model that is identical for long-wave phenomena to that obtained here. However, asymptotic completeness has not yet been proved for such 'infinite dimensional' centre manifold models as we derive and as others justify using formal heuristics.) With this proviso, a low-dimensional model of the system is justified using centre manifold techniques. The critical aspect of the theory is that it provides a systematic and flexible framework for constructing those solutions of the governing Navier–Stokes equations that emerge when viscosity damps most of the lateral shear modes.

Denote the physical fields by $\boldsymbol{v}(t) = (\eta, u_1, u_2, v, p)$. Centre manifold theory guarantees that there exist physical fields described by functions $\boldsymbol{V}$ and $\boldsymbol{G}$ of the critical modes where the critical modes evolve in time, that is, (32) here becomes

$$\boldsymbol{v}(t) = \boldsymbol{V}(\eta, \bar{u}_1, \bar{u}_2) \quad \text{such that} \quad \frac{\partial}{\partial t}\begin{bmatrix}\eta\\ \bar{u}_1\\ \bar{u}_2\end{bmatrix} = \boldsymbol{G}(\eta, \bar{u}_1, \bar{u}_2), \tag{46}$$

where there is implicit dependence upon the parameters (ϵ, γ, Gr), which are treated as small constants, and where $\bar{u}_i$ are depth-averaged lateral velocities defined precisely

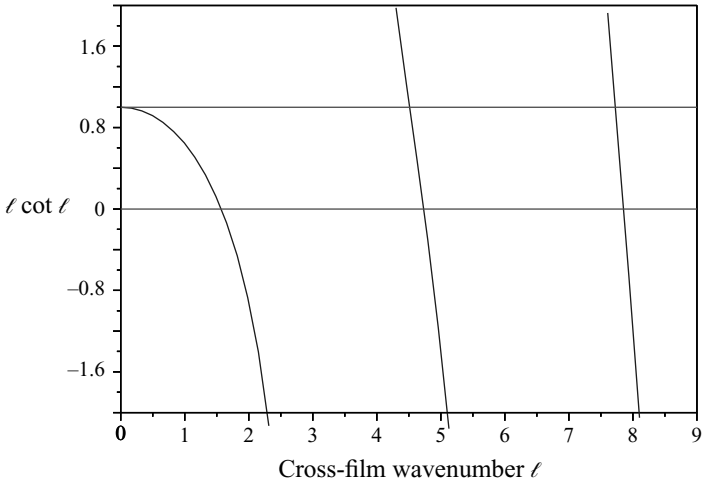

FIGURE 3. Curve $\ell \cot \ell$ versus cross-film wavenumber ℓ and its intersections with 0 and 1 confirming the spectral gap for $0 \leqslant \gamma \leqslant 1$ and that there is a smooth analytic dependence of ℓ^2 on γ in the solution of $\ell \cot \ell = 1 - \gamma$.

as

$$\bar{u}_i = \frac{1}{\eta} \int_0^\eta u_i (1 - k_{i'} y) \, \mathrm{d}y. \tag{47}$$

This definition ensures that the fluid flux over a point on the substrate is simply $\eta \bar{\boldsymbol{u}}$. We proceed to find functions $\boldsymbol{V}$ and $\boldsymbol{G}$ such that the evolving fluid fields $\boldsymbol{v}(t)$ as described by (46) are actual solutions of the Navier–Stokes equations (34)–(35) satisfying boundary conditions (36)–(39).

The major modifications are found to be successful. A key part of our analysis is that the tangential stress boundary condition (29) can have major modifications to (39) and still form a useful base for physical modelling with centre manifold techniques. The critical issue is whether the physical problem with $\gamma = 1$ is accessible by power series in γ about the artificial case of $\gamma = 0$. Here, we consider briefly just the linear dynamics of the lateral shear velocity $u(y, t)$ to show evidence of the convergence of this power series; in § 5 we show further evidence of convergence for other parts of the model. The equations for the dynamics of the lateral shear modes are

$$Re \, \frac{\partial u}{\partial t} = \frac{\partial^2 u}{\partial y^2} \quad \text{with} \quad u|_{y=0} = 0, \quad \frac{\partial u}{\partial y} = \frac{1-\gamma}{\eta} u \quad \text{on } y = \eta. \tag{48}$$

For all γ, separation of variables straightforwardly leads us to the complete solution

$$u = \sum_{n=0}^{\infty} \exp(\lambda_n t) \sin(\ell_n y/\eta) \quad \text{where} \quad \lambda_n(\gamma) = -\frac{\ell_n^2}{Re \, \eta^2}$$

and the non-dimensional wavenumbers $\ell_n(\gamma)$ are the solutions of $\ell \cot \ell = 1 - \gamma$. Figure 3 shows how the square of the wavenumbers ℓ_n are analytic functions of the parameter γ, hence so is $\lambda_0 = -\ell_0^2/(Re \, \eta^2)$, and so will be represented by a power series convergent in some domain: our model involves the viscous decay of the fundamental shear mode, hence involves λ_0 and thus is based upon the branch emanating from $\ell = 0$ for $\gamma = 0$ and reaching $\ell = \pi/2$ for $\gamma = 1$. Evidently this power series should converge at $\gamma = 1$; we present further evidence in § 5.

Furthermore, from $\gamma = 0$ to $\gamma = 1$ there is a wide spectral gap between the model's rate of evolution, $0 \geqslant Re\,\eta^2\lambda_0 \geqslant -\pi^2/4$, and the leading transient's rate of evolution, $-20.19 \geqslant Re\,\eta^2\lambda_1 \geqslant -9\pi^2/4 = -22.21$. The spectral gap ratio is $\lambda_1/\lambda_0 \geqslant 9$ throughout. This spectral gap underlies our modelling of thin fluid dynamics (Roberts 1998). (Indeed theorem 4.1 of Gallay's (1993) also applies to this situation to ensure the existence of a type of centre manifold based at $\gamma = 1$. The difference is that the theory only assures us the centre manifold has its first nine derivatives continuous (from the spectral gap). However, our practical construction of the model is far easier when based on the zero eigenvalues found at $\gamma = 0$ and so we use this as the base.)

Moreover, the spectral gap from the resolved mode, the left-most branch in figure 3, to the first neglected lateral shear mode, the branch with $\ell \approx 5$ in figure 3, indicates the time scales that the model will resolve. The model will not resolve dynamics on the time scale of this first neglected shear mode. This mode has a decay rate of roughly $-20/(Re\,\eta^2)$ and so the model resolves dynamics on time scales longer than roughly $Re\,\eta^2/20$. In contrast, lubrication models such as (1) neglect the leading branch in figure 3 and so only resolve dynamics of an order of magnitude longer time scales.

To solve by iteration, we construct the centre manifold model, $\boldsymbol{V}$ and $\boldsymbol{G}$, by iteration using computer algebra (Roberts 1997). (At the time of writing the source code for the computer algebra may be downloaded from http://www.sci.usq.edu.au/staff/aroberts/CAthreed.red). Based upon driving the residuals of the governing equations to zero, the critical calculations are straightforward to check in our approach. In outline, suppose that an approximation $\tilde{\boldsymbol{V}}$ and $\tilde{\boldsymbol{G}}$ has been found, and let $\boldsymbol{V}'$ and $\boldsymbol{G}'$ denote corrections we seek in order to improve $\tilde{\boldsymbol{V}}$ and $\tilde{\boldsymbol{G}}$. Substituting

$$\boldsymbol{v} = \tilde{\boldsymbol{V}} + \boldsymbol{V}', \quad \frac{\partial}{\partial t}\begin{bmatrix}\eta\\ \bar{u}_1\\ \bar{u}_2\end{bmatrix} = \tilde{\boldsymbol{G}} + \boldsymbol{G}',$$

into (34)–(35) and its boundary conditions, then rearranging, dropping products of corrections, and using the linear approximation wherever factors multiply corrections (see Roberts 1997, for more details), we obtain a system of linear equations for corrections that improve $\tilde{\boldsymbol{V}}$ and $\tilde{\boldsymbol{G}}$. The resulting system of equations is in the homological form

$$\mathscr{L}\boldsymbol{V}' + \boldsymbol{A}\boldsymbol{G}' = \tilde{\boldsymbol{R}}, \tag{49}$$

where $\mathscr{L}$ is the linear operator on the left-hand side of system (42)–(44), $\boldsymbol{A}$ is a matrix, and $\tilde{\boldsymbol{R}}$ is the residual of the governing PDEs (34)–(35) and their boundary conditions (36)–(39) using the reigning approximations $\tilde{\boldsymbol{V}}$ and $\tilde{\boldsymbol{G}}$. The procedure for solving the homological equation (49), familiar from the method of multiple scales, is as follows: first, choose $\boldsymbol{G}'$ such that $\tilde{\boldsymbol{R}} - \boldsymbol{A}\boldsymbol{G}'$ is in the range of $\mathscr{L}$; secondly, solve $\mathscr{L}\boldsymbol{V}' =$ right-hand side, making the solution satisfy the boundary conditions (36)–(39) and the definitions (47). Then regard $\tilde{\boldsymbol{V}} + \boldsymbol{V}'$ and $\tilde{\boldsymbol{G}} + \boldsymbol{G}'$ as the new approximation $\tilde{\boldsymbol{V}}$ and $\tilde{\boldsymbol{G}}$, respectively. Repeat the iteration until satisfied with the approximation. The ultimate purpose is to make the residual $\tilde{\boldsymbol{R}}$ become zero to a specified order in small parameters, then the approximation theorem (Carr 1981) in centre manifold theory assures us that the low-dimensional model has the same order of error.

This correspondence between residual and error is a critical and important feature of the centre manifold approach: we solve the governing physical equations in a systematic framework with no assumptions about the detailed structure of the fluid field; in contrast, other methods assume at the outset that the fluid flows with some

prescribed shear, usually parabolic. However, for example, the numerical solutions by Malamataris, Vlachogiannis & Bontozoglou (2002) of the full Navier–Stokes equations show that under the front of solitary waves, such as those shown in figure 6, the velocity profile is markedly not parabolic, see their figure 7. We also show (figure 10) the non-parabolic velocity field under a hydraulic jump observed in experiments (e.g. Bohr *et al.* 1996). Thus, our centre manifold modelling encompasses a much wider range of flows than other approaches.

5. The high-order model of film flow

The computer algebra program derives the physical fields of slowly varying thin-film fluid flow, and also obtains the evolution thereon as a set of coupled partial differential equations for the evolution of the film thickness η and the averaged lateral velocities $\bar{\boldsymbol{u}}$.

The description of the velocity and pressure fields rapidly becomes very complicated as more terms are computed in their approximations. Thus, here we first record the dominant terms in their expressions as an example to aid later discussion. Computing to low order in the small parameters, we determine the pressure and velocity fields in terms of the parameters and a scaled normal coordinate $Y = y/\eta$:

$$\begin{aligned} p = {} & -\epsilon\, We\,\kappa - \epsilon^2\, We\,\nabla^2\eta + \epsilon\eta^{-1}\nabla\eta\cdot\bar{\boldsymbol{u}}(Y-1)(2+\gamma/2) - \epsilon^2\, We\,\eta\kappa_2 \\ & + \epsilon\nabla\cdot\bar{\boldsymbol{u}}\,(\gamma(Y-3)/2 - 2(Y+1)) + Gr\,\eta g_n(Y-1) \\ & + O(\epsilon^3 + \bar{u}^3 + Gr^{3/2}, \gamma^2); \end{aligned} \tag{50}$$

$$\begin{aligned} \boldsymbol{u} = {} & \bar{\boldsymbol{u}}(2Y - \gamma(Y^3 - Y/2)) + \eta^2(\epsilon^2\, We\,\nabla\kappa + Gr\,\boldsymbol{g}_s)\left(-\tfrac{3}{80}\gamma Y^5\right. \\ & \left. + \tfrac{23}{240}\gamma Y^3 - \tfrac{17}{480}\gamma Y + \tfrac{1}{4}Y^3 - \tfrac{1}{2}Y^2 + \tfrac{5}{24}Y\right) \\ & + \epsilon\eta\kappa\bar{\boldsymbol{u}}\left(\tfrac{3}{20}\gamma Y^5 - \tfrac{1}{2}\gamma Y^4 - \tfrac{23}{60}\gamma Y^3 + \tfrac{1}{4}\gamma Y^2 + \tfrac{13}{120}\gamma Y\right. \\ & \left. - \tfrac{1}{2}Y^3 + Y^2 + \tfrac{11}{12}Y\right) + \epsilon\eta\boldsymbol{K}\cdot\bar{\boldsymbol{u}}\left(\tfrac{3}{10}\gamma Y^5 + \tfrac{17}{60}\gamma Y^3\right. \\ & \left. - \tfrac{19}{60}\gamma Y - Y^3 - \tfrac{5}{6}Y\right) + O(\epsilon^3 + \bar{u}^3 + Gr^{3/2}, \gamma^2); \end{aligned} \tag{51}$$

$$\begin{aligned} v = {} & \epsilon\nabla\eta\cdot\bar{\boldsymbol{u}}(\gamma(-3Y^4 + Y^2)/4 + Y^2) \\ & + \epsilon\eta\nabla\cdot\bar{\boldsymbol{u}}(\gamma(Y^4 - Y^2)/4 - Y^2) \\ & + O(\epsilon^3 + \bar{u}^3 + Gr^{3/2}, \gamma^2); \end{aligned} \tag{52}$$

where g_n is the component of gravity in the direction normal to the substrate. The error terms in these and later expressions involve $\bar{u} = \|\bar{\boldsymbol{u}}\|$, and then $O(\epsilon^p + \bar{u}^q + Gr^m, \gamma^n)$ encompasses all terms which

either contain p' lateral derivatives and curvature factors, q' lateral velocity factors, and m' gravity forcing factors where $p'/p + q'/q + m'/m \geqslant 1$,

or contain a factor $\gamma^{n'}$ for $n' \geqslant n$.

These orders of errors come via the approximation theorem from the order of residuals in solving the fluid equations (34)–(39). Note that we chose to derive expressions for the fluid fields which have the same absolute order of error. One may prefer instead to derive expressions to the same relative order of error; finding an extra order in the pressure p and vertical velocity v for example, but this would require scaling the continuity and and the vertical momentum equation. Whereas it is arguable that there may be some benefit in doing this rescaling in deriving the lubrication model, there is no benefit here because such extra terms just add complication without improving the model's lateral momentum equation below. Thus, using the above fluid fields with their absolute order of errors, the corresponding evolution to this order of accuracy

	$\bar{\boldsymbol{u}}/\eta^2$	$\boldsymbol{g}_s$	$\bar{\boldsymbol{u}}\kappa/\eta$
1	0	+0.75000	−1.50000
γ	−3.00000	+0.10000	+0.60000
γ^2	+0.60000	−0.03286	−0.10286
γ^3	−0.06857	+0.00571	0
γ^4	0	−0.00032	+0.00321
γ^5	+0.00128	−0.00009	−0.00024
γ^6	−0.00008	+0.00002	−0.00014
γ^7	−0.00004	+0.00000	+0.00003

TABLE 1. Some higher-order terms in the series expansions in γ of selected coefficients in the low-dimensional model (58) showing that these expansions are effectively summed at $\gamma = 1$.

is

$$\frac{\partial \eta}{\partial t} = -\epsilon \nabla \cdot (\eta \bar{\boldsymbol{u}}) + O\left(\epsilon^3 + \bar{u}^3 + Gr^{3/2}, \gamma^2\right), \tag{53}$$

$$\begin{aligned} Re\,\frac{\partial \bar{\boldsymbol{u}}}{\partial t} = {} & (\epsilon^2\, We\, \nabla\kappa + Gr\, \boldsymbol{g}_s)\left(\tfrac{3}{4} + \tfrac{1}{10}\gamma\right) - \epsilon\eta^{-1}\boldsymbol{K}\cdot\bar{\boldsymbol{u}}\left(3 - \tfrac{6}{5}\gamma\right) \\ & - \epsilon\eta^{-1}\kappa\bar{\boldsymbol{u}}\left(\tfrac{3}{2} - \tfrac{3}{5}\gamma\right) - 3\eta^{-2}\bar{\boldsymbol{u}}\gamma + O\left(\epsilon^3 + \bar{u}^3 + Gr^{3/2}, \gamma^2\right). \end{aligned} \tag{54}$$

Throughout, $\boldsymbol{K}$ is the curvature tensor, which in the special coordinate system chosen to fit the substrate takes the diagonal form

$$\boldsymbol{K} = \begin{pmatrix} k_1 & 0 \\ 0 & k_2 \end{pmatrix}. \tag{55}$$

Although derived in the special coordinate system, the above and later more refined results in this section are all written in a coordinate free form. The differential operators that appear are those of the substrate. In the special orthogonal coordinate system, they involve the substrate scale factors m_i as in the Laplacian (17).

To recover the original model, we must set $\gamma = 1$ so that (39) reverts to the physically correct stress-free boundary condition. However, the above model has errors of $O(\gamma^2)$ which will be rather large at $\gamma = 1$. Thus, we proceed to use computer algebra to compute sufficient higher order terms in γ to evaluate the model reasonably accurately.

In the asymptotic expansions, every coefficient is a series in γ, and the ratios of the coefficients of γ^{n-1} to γ^n in all such series appear to be greater than about 1.5 for $n > 2$ from further calculation. That is, the radii of convergence of the various series in γ are greater than about 1.5. Table 1 shows the coefficients of the γ series of some terms in a higher-order version of the low dimensional model (54). Evidently, the convergence of at least these series' is very good – we expect five decimal place accuracy from the terms shown and similar for the other coefficients. Roberts (1996, 1998) and Mei *et al.* (2003) report similar convergence in other similar problems. Hence, we justifiably substitute $\gamma = 1$ into the series of every coefficient to obtain the physical model. Hereinafter, we calculate every coefficient in the evolution from the terms in the series up to and including those of order γ^7. Computer memory and time limitations preclude us from computing higher orders in γ for the wide range of physical interactions we resolve here. We also now set $\epsilon = 1$ to recover the unscaled model of the original dynamics. With higher-order corrections in γ, the

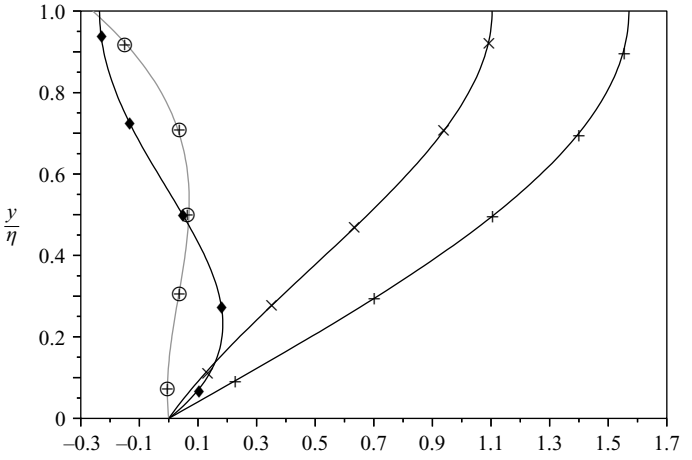

FIGURE 4. The normal structure of the lateral velocity field (51): +, component $\propto \bar{\boldsymbol{u}}$; $\times$, component $\propto k_{i'}\boldsymbol{u}_i$; $\circ$, component $\propto k_i\boldsymbol{u}_i$; and $\diamond$, $10\times$ component $\propto We\,\nabla\kappa + Gr\,\boldsymbol{g}_s$.

low-dimensional model (54) then becomes the model (6) discussed briefly in § 1. Based on the above evidence, the coefficients in the models given in § 1 and the models we discuss here in after should be accurate to at least four decimal places.

The expressions (50)–(52), when $\gamma = \epsilon = 1$, approximate the physical state of the fluid flow corresponding to a given η, $\bar{u}_1$ and $\bar{u}_2$. Using the accurate expressions, determined by computing to γ^7, figure 4 shows the normal cross-film structure of the lateral velocity field $\boldsymbol{u}$. The +-curve shows the fundamental structure of the lateral velocity in the normal direction; qualitatively, it is dominantly parabolic, but it is actually indistinguishable from the trigonometric $(\pi/2)\sin(\pi Y/2)$ as required for the viscous decay of the gravest lateral shear mode (Roberts 1996), and thus is slightly faster at the free surface than the parabolic profile with the same flux. The $\times$-curve shows that in order to maintain the flux $\bar{\boldsymbol{u}}$ along a trough, $k_{i'} > 0$ (recall that $i' = 3 - i$), the flow $u_i(Y)$ has to be proportionally faster. The $\circ$-curve shows that flow curving upward, around an internal corner, is slower at the free surface and conversely faster for flow around an external corner; part of this effect could be attributed to solid-body rotation being the dissipation free mode for turning a corner. Lastly, the $\diamond$-curve, exaggerated by a factor of ten, shows the very small adjustment made to the profile when the flow is driven by gravity or lateral pressure gradients – observe the velocity at the free surface will decrease slightly so that when lateral forces exactly balance the drag on the substrate the profile will then be the familiar parabolic Nusselt flow. These show how just some of the physical processes affect the details of the physical fields and thus indirectly influence the evolution.

The shear stress on the substrate is of interest:

$$\boldsymbol{\tau}_y = 2.467\frac{\bar{\boldsymbol{u}}}{\eta} + 0.1775\,\eta(We\,\nabla\kappa + Gr\,\boldsymbol{g}_s) + (\kappa\boldsymbol{I} - 3.609\,\boldsymbol{K})\cdot\bar{\boldsymbol{u}} + O\left(\partial_x^3 + \bar{u}^3 + Gr^{3/2}\right). \quad (56)$$

The first term is just the viscous drag on a flat substrate. The next is the enhanced stress transmitted to the substrate when the fluid is driven by a body force or pressure gradients, equivalently. The third and last term accounts for the effects of curvature on the velocity field affecting the velocity profile near the bed.

With computer algebra we readily compute a more comprehensive model which is higher order in lateral derivatives ϵ, gravitational forcing Gr, and overall velocity $\bar{u}$.

Atherton & Homsy (1973), Lange, Nandakumar & Raszillier (1999) and Roy *et al.* (2002) similarly considered high-order models of thin-film flows obtained via computer algebra, but only in the lubrication approximation. Computing to the next order in spatial gradients ϵ, velocity field $\bar{u}$, and gravitational forcing Gr, we write the model as (recall $\zeta = \eta - \kappa\eta^2/2 + k_1k_2\eta^3/3$ is proportional to the amount of fluid locally 'above' a small patch of the substrate)†

$$\frac{\partial \zeta}{\partial t} = -\nabla\cdot(\eta\bar{\boldsymbol{u}}), \tag{57}$$

$$\begin{aligned}
Re\,\frac{\partial \bar{\boldsymbol{u}}}{\partial t} = &-\left[\frac{\pi^2}{4}\frac{\bar{\boldsymbol{u}}}{\eta^2} + (2\boldsymbol{K}+\kappa\boldsymbol{I})\cdot\frac{\bar{\boldsymbol{u}}}{\eta}\right.\\
\text{(drag)}\qquad &\left.+(3.2974\,\boldsymbol{K}\cdot\boldsymbol{K} - 1.1080\,\kappa\boldsymbol{K} + 0.6487\,\kappa_2\boldsymbol{I})\cdot\bar{\boldsymbol{u}}\right]\\
\text{(tension)}\qquad &+We\left[\frac{\pi^2}{12}\nabla(\kappa+\eta\kappa_2+\nabla^2\eta) + 1.0779\,\eta\boldsymbol{K}\cdot\nabla\kappa - 0.4891\,\eta\kappa\nabla\kappa\right]\\
\text{(gravity)}\qquad &+Gr\left[\frac{\pi^2}{12}(\boldsymbol{g}_s + g_n\nabla\eta) + 0.2554\,\eta\boldsymbol{K}\cdot\boldsymbol{g}_s - 0.4891\,\eta\kappa\boldsymbol{g}_s)\right]\\
\text{(advect)}\qquad &-Re\,[1.3464\,\bar{\boldsymbol{u}}\cdot\nabla\bar{\boldsymbol{u}} + (0.1483\,\bar{\boldsymbol{u}}\cdot\nabla\eta/\eta + 0.1577\,\nabla\cdot\bar{\boldsymbol{u}})\,\bar{\boldsymbol{u}}]\\
\text{(viscous)}\qquad &+\frac{4.0930}{\eta^{0.8348}}\nabla[\eta^{0.4886}\nabla\cdot(\eta^{0.3461}\bar{\boldsymbol{u}})] - \frac{1}{\eta^{0.4377}}\nabla\times\left[\frac{1}{\eta^{1.0623}}\nabla\times\left(\eta^{3/2}\bar{\boldsymbol{u}}\right)\right]\\
&+0.9377\frac{1}{\eta}\nabla\eta\times(\nabla\times\bar{\boldsymbol{u}}) - 2.4099\frac{\bar{\boldsymbol{u}}}{\eta^{0.8299}}\nabla^2(\eta^{0.8299})\\
&+O(\nabla^4 + \bar{u}^4 + Gr^2),
\end{aligned} \tag{58}$$

where the differential operators are those of the substrate coordinate system, noting in particular that (Batchelor 1979, p. 599)

$$\begin{aligned}
\nabla\times\bar{\boldsymbol{u}} &= \boldsymbol{e}_3\frac{1}{m_1m_2}\left[\frac{\partial(m_2\bar{u}_2)}{\partial x_1} - \frac{\partial(m_1\bar{u}_1)}{\partial x_2}\right],\\
\nabla\times(\boldsymbol{e}_3\omega) &= \boldsymbol{e}_1\frac{1}{m_2}\frac{\partial\omega}{\partial x_2} - \boldsymbol{e}_2\frac{1}{m_1}\frac{\partial\omega}{\partial x_1},\\
\bar{\boldsymbol{u}}\cdot\nabla\bar{\boldsymbol{u}} &= \boldsymbol{e}_1\left[\bar{\boldsymbol{u}}\cdot\nabla\bar{u}_1 + \frac{\bar{u}_2}{m_1m_2}\left(\bar{u}_1\frac{\partial m_1}{\partial x_2} - \bar{u}_2\frac{\partial m_2}{\partial x_1}\right)\right]\\
&\quad + \boldsymbol{e}_2\left[\bar{\boldsymbol{u}}\cdot\nabla\bar{u}_2 + \frac{\bar{u}_1}{m_1m_2}\left(\bar{u}_2\frac{\partial m_2}{\partial x_1} - \bar{u}_1\frac{\partial m_1}{\partial x_2}\right)\right].
\end{aligned}$$

Observe that (57) conserves fluid. In the above model, (58), for the average lateral velocity field, we identify the apparent physical source of the terms in the various lines by the key words on the left-hand side. Generally the viscous drag on the bed, surface tension forces and gravitational forcing show some subtle effects of the curvature of the substrate. In faster flows of higher Reynolds number, the most usually modelled part of the advection terms, the self-advection term $\bar{\boldsymbol{u}}\cdot\nabla\bar{\boldsymbol{u}}$, has the definite coefficient 1.3464. However, note that some of the self-advection is also encompassed within the $(\nabla\cdot\bar{\boldsymbol{u}})\bar{\boldsymbol{u}}$ term. This modelling settles (see for example Prokopiou *et al.* 1991, equation (19)) the correct theoretical value for this and other coefficients. It

† Some of the constants that appear here are tentatively identified: $1.0779 = (\pi^2+16)/24$, $0.4891 = (\pi^2-4)/12$, $2.4099 = \pi^2/7+1$ and perhaps $4.0930 = (8\pi^2+7)/21$.

seems most natural to express the lateral damping via viscosity in a mixed form involving both the general grad-div operator and the curl-curl operator (recall the vector identity $\nabla^2\boldsymbol{u} = \nabla(\nabla\cdot\boldsymbol{u}) - \nabla\times(\nabla\times\boldsymbol{u})$). The involvement of fractional powers of the film thickness within the scope of these operators is a convenient way of reducing the number of terms within the equation; as yet we have not discerned any interesting physical significance to this arrangement. You may truncate the above model in a variety of consistent ways depending upon the parameter regimes of the application you wish to consider.

Lubrication models such as (1) may be derived from (57)–(58). Obtain simple low-order accurate models simply by the adiabatic approximation of balancing the drag terms, dominantly $(\pi^2/4)\bar{\boldsymbol{u}}/\eta^2$, against the driving forces expressed by the surface tension and gravity terms. This then expresses the average velocity field $\bar{\boldsymbol{u}}$ as a function of the film thickness η. Substitute this expression into the conservation of fluid equation, (57), to form a lubrication model. Form higher-order more sophisticated models by taking into account the consequent time dependence of the weaker previously neglected terms in (58). Any resultant lubrication model is correct because rational mathematical modelling is transitive: a coarser model of a model of some dynamics is the same as the coarser model derived directly.

Slower flow occurs when, in a specific application, the velocity field is predominantly driven by surface tension acting because of curvature gradients, whence $\bar{u} = O(\nabla\kappa)$. The lateral velocities are significantly damped by viscous drag on the substrate. In this case, truncate (58) to

$$Re\,\frac{\partial\bar{\boldsymbol{u}}}{\partial t} = -\left[\frac{\pi^2}{4}\frac{\bar{\boldsymbol{u}}}{\eta^2} + (2\boldsymbol{K}+\kappa\boldsymbol{I})\cdot\frac{\bar{\boldsymbol{u}}}{\eta}\right] + We\left[\frac{\pi^2}{12}\nabla\tilde{\kappa} + 1.0779\,\eta\boldsymbol{K}\cdot\nabla\kappa - 0.4891\,\eta\kappa\nabla\kappa\right]$$
$$+ Gr\left[\frac{\pi^2}{12}(\boldsymbol{g}_s + g_n\nabla\eta) + 0.2554\,\eta\boldsymbol{K}\cdot\boldsymbol{g}_s - 0.4891\,\eta\kappa\,\boldsymbol{g}_s)\right] + O(\nabla^4 + \bar{u}^2 + Gr^2); \tag{59}$$

the difference is that many terms in (58) are swept into the $\bar{u}^2$ term in the order of error term in the simpler model (59). That is, you may adjust the dynamical model (58) to suit a particular application by choosing an appropriate consistent truncation.

Order one gradients are encompassed by the model (58). 'Long wave' models such as (58) and (59) are based on the assumption that the lateral spatial gradients are small. We here quantify what a 'small gradient' means in this context following similar arguments for the Taylor model of shear dispersion (Mercer & Roberts 1990; Watt & Roberts 1995). We modify a simpler version of the computer algebra derivation to find the centre manifold model of the linear dynamics about a stationary constant thickness fluid with surface tension but no gravity: $\eta = \eta_0 + \alpha\eta' + O(\alpha^2)$ and $\boldsymbol{u} = \alpha\boldsymbol{u}' + O(\alpha^2)$ where†

$$\frac{\partial\eta'}{\partial t} = -\eta_0\nabla\cdot\bar{\boldsymbol{u}}' + O(\alpha), \tag{60}$$

$$\frac{\partial\bar{\boldsymbol{u}}'}{\partial t} = \frac{1}{\eta_0^2}\left[-2.47 + 4.09\,\eta_0^2\nabla^2 + 0.734\,\eta_0^4\nabla^4 + 0.0611\,\eta_0^6\nabla^6 + 0.0223\,\eta_0^8\nabla^8\right]\bar{\boldsymbol{u}}'$$
$$+ \frac{We}{\eta_0^3}\left[0.822\,\eta_0^3\nabla^3 + 0.116\,\eta_0^5\nabla^5 + 0.00168\,\eta_0^7\nabla^7 + 0.00298\,\eta_0^9\nabla^9\right]\eta'$$
$$+ O(\alpha, \nabla^{10}). \tag{61}$$

† The coefficients in the linear model (61) come from evaluating at $\gamma = 1$ an expansion with errors $O(\gamma^7)$. The coefficients used here should be accurate as discussed earlier and demonstrated in table 1.

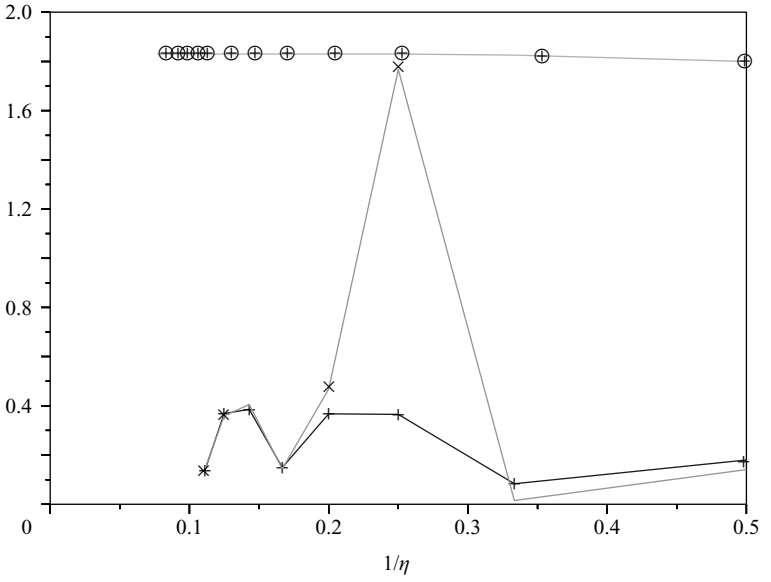

FIGURE 5. Domb–Sykes plot of the formal expansions (61) extended to $O(\nabla^{20})$, $\times$ and $+$, showing that the radius of convergence, $1/n \to 0$, may be roughly in the range 1/0.15 to 1/0.35. $\oplus$, the Domb–Sykes plot for the analogous lubrication model (63), showing its radius of convergence is 1/1.83.

Evidently, the linear dynamics are a formal expansion in $\eta_0^2\nabla^2$. This expansion converges when the lateral gradients are not too steep. Suppose that locally a solution has spatial structure approximated by an exponential variation, say $\eta' \propto \mathrm{e}^{\nu x}$ for possibly complex ν, then the above expansions become power series expansion in $\eta_0^2\nu^2$. The Domb–Sykes plot (Mercer & Roberts 1990) of the ratio of successive coefficients in figure 5 suggests that the power series converges for $\eta_0^2\nu^2$ less than something roughly in the range 1/0.15 to 1/0.35. The constant sign of the coefficients in (61) indicates the convergence limiting singularity occurs for real steep gradients. However, the strong period 3 oscillations in the Domb–Sykes plot of the ratio indicates that a complex conjugate pair of singularities occurs at an angle of $\pm\pi/3$ to the real axis at nearly the same 'distance'. The generalization of the Domb–Sykes plot to cater for multiple comparable limiting singularities (Watt & Roberts 1995) indicates that the three singularities are at a distance about 1/0.28; that is, for any quantity w, the magnitude of the logarithmic derivative of the lateral structure

$$|\nabla(\log w)| = \left|\frac{\nabla w}{w}\right| < \frac{1.9}{\eta}, \tag{62}$$

for the model to converge. For example, apply this limit to the surface thickness, $w = \eta$, to deduce that the steepness of the fluid variations $|\nabla\eta| < 1.9$, and that accurate approximation is achieved for steepnesses significantly less than this rough limit. Hence, steepnesses up to about one should be reasonably well represented by those low-order terms appearing in the model (58).

For interest, we also investigated the analogous but poorer spatial resolution of the lubrication model (1) of thin-film flow (e.g. Roy *et al.* 2002). The analogous high-order

but linear model is

$$\frac{\partial \eta'}{\partial t} = We\left[-0.333\,\eta_0^3\nabla^4 - 0.6\,\eta_0^5\nabla^6 - 1.09\,\eta_0^7\nabla^8 - 2.00\,\eta_0^9\nabla^{10} - 3.67\,\eta_0^{11}\nabla^{12}\right]\eta' + O(\alpha, \nabla^{14}). \tag{63}$$

Continuing this expansion to errors $O(\nabla^{30})$, see in its Domb–Sykes plot in figure 5 that this power series converges only for much less rapid variations than the model (58). For example, the fluid thickness steepness $|\nabla\eta| < 0.74$, and so should be less than about a third, say, in order for the usual first term in the lubrication model $\eta_t = \frac{1}{3}\,We\,\nabla\cdot(\eta^3\nabla^3\eta)$ to be reasonable. Thus, expect the model (58) developed here to resolve spatial structure roughly three times as fine as a lubrication model could.

6. The model on various specific substrates

The model (57)–(58) contains many terms as a consequence of the wide range of physical interactions encompassed by the model. It is not obvious how the model will appear in any particular geometry. Thus in this section we record the model for four common substrate shapes: flat, cylindrical, channel and spherical. The models are given in terms of elementary derivatives rather than vector operators for easier use in specific problems. Some example flows in each case illustrate the dynamics resolved and we also make some quantitative comparisons with other models.

6.1. *Flow on a flat substrate resolves a radial hydraulic jump*

The simplest example is the flow on a flat substrate. We discuss wave transitions, compare solitary waves, simulate Faraday waves, explore divergence and vorticity in the linearized dynamics, and demonstrate that modelling the inertia enables us to resolve hydraulic jumps in a radial flow.

On a flat substrate, use a Cartesian coordinate system (x, y) and let the mean lateral velocity $\bar{\boldsymbol{u}}$ have components $\bar{u}$ and $\bar{v}$, respectively (note that in this subsection y is a tangential coordinate, not the normal coordinate as used before). The substrate has scale factors $m_1 = m_2 = 1$, and curvatures $k_1 = k_2 = 0$. The model (57)–(58) becomes, where g_n is the direction cosine of gravity normal to the substrate into the fluid layer and where subscripts on η denote partial derivatives,

$$\frac{\partial \eta}{\partial t} \approx -\frac{\partial(\eta\bar{u})}{\partial x} - \frac{\partial(\eta\bar{v})}{\partial y}, \tag{64}$$

$$\begin{aligned} Re\,\frac{\partial \bar{u}}{\partial t} \approx{}& -\frac{\pi^2}{4}\frac{\bar{u}}{\eta^2} + \frac{\pi^2}{12}[Gr(g_x + g_n\eta_x) + We(\eta_{xxx} + \eta_{xyy})] \\ & - Re\left[1.5041\,\bar{u}\frac{\partial \bar{u}}{\partial x} + 1.3464\,\bar{v}\frac{\partial \bar{u}}{\partial y} + 0.1577\,\bar{u}\frac{\partial \bar{v}}{\partial y} + 0.1483\frac{\bar{u}}{\eta}\left(\bar{u}\eta_x + \bar{v}\eta_y\right)\right] \\ & + \left[4.0930\frac{\partial^2 \bar{u}}{\partial x^2} + \frac{\partial^2 \bar{u}}{\partial y^2} + 3.0930\frac{\partial^2 \bar{v}}{\partial x\,\partial y} + 4.8333\frac{\eta_x}{\eta}\frac{\partial \bar{u}}{\partial x} + \frac{\eta_y}{\eta}\frac{\partial \bar{u}}{\partial y}\right. \\ & \quad + 1.9167\frac{\eta_x}{\eta}\frac{\partial \bar{v}}{\partial y} + 1.9167\frac{h_y}{\eta}\frac{\partial \bar{v}}{\partial x} \\ & \quad + \left(-0.5033\frac{\eta_y^2}{\eta^2} - \frac{\eta_{yy}}{2\eta} + 0.1061\frac{\eta_x^2}{\eta^2} - 0.5834\frac{\eta_{xx}}{\eta}\right)\bar{u} \\ & \quad \left. + \left(0.6094\frac{\eta_y\eta_x}{\eta^2} - 0.0833\frac{\eta_{xy}}{\eta}\right)\bar{v}\right], \end{aligned} \tag{65}$$

$$
\begin{aligned}
Re\,\frac{\partial \bar{v}}{\partial t} \approx & -\frac{\pi^2}{4}\frac{\bar{v}}{\eta^2} + \frac{\pi^2}{12}[Gr(g_y + g_n\eta_y) + We(\eta_{xxy} + \eta_{yyy})] \\
& - Re\left[1.3464\,\bar{u}\frac{\partial \bar{v}}{\partial x} + 1.5041\,\bar{v}\frac{\partial \bar{v}}{\partial y} + 0.1577\,\bar{v}\frac{\partial \bar{u}}{\partial x} + 0.1483\frac{\bar{v}}{\eta}\left(\bar{u}\eta_x + \bar{v}\eta_y\right)\right] \\
& + \left[\frac{\partial^2 \bar{v}}{\partial x^2} + 4.0930\frac{\partial^2 \bar{v}}{\partial y^2} + 3.0930\frac{\partial^2 \bar{u}}{\partial x \partial y}\right. \\
& \quad + 4.8333\frac{\eta_y}{\eta}\frac{\partial \bar{v}}{\partial y} + \frac{\eta_x}{\eta}\frac{\partial \bar{v}}{\partial x} + 1.9167\frac{\eta_x}{\eta}\frac{\partial \bar{u}}{\partial y} + 1.9167\frac{h_y}{\eta}\frac{\partial \bar{u}}{\partial x} \\
& \quad + \left(-0.5033\frac{\eta_x^2}{\eta^2} - \frac{\eta_{xx}}{2\eta} + 0.1061\frac{\eta_y^2}{\eta^2} - 0.5834\frac{\eta_{yy}}{\eta}\right)\bar{v} \\
& \quad \left. + \left(0.6094\frac{\eta_y\eta_x}{\eta^2} - 0.0833\frac{\eta_{xy}}{\eta}\right)\bar{u}\right]. \qquad (66)
\end{aligned}
$$

Observe that the substrate drag, gravitational and surface-tension terms are straightforward. However, the self-advection terms exhibit subtle interactions between the components of the velocity fields owing to the specific shape of the velocity profiles. Further subtleties occur in the viscous terms which not only show explicitly a differential lateral dispersion of momentum, but also a complex interaction with variations in the free-surface shape.

Ruyer-Quil & Manneville (2000) also derive a model for three-dimensional flow on a flat plate using Galerkin projection. Their model, equations (53)–(54) in their work, is based on the flow down an inclined plate and consequently is anisotropic; for example, their model has no second-order viscous dissipation for any flow in the direction across the slope. Our isotropic model above retains second-order dissipation independent of the dominant direction of flow.

As used next and in agreement with Roberts (1996), this model simplifies considerably for two-dimensional flow to

$$
\frac{\partial \eta}{\partial t} \approx -\frac{\partial(\eta\bar{u})}{\partial x}, \qquad (67)
$$

$$
\begin{aligned}
Re\,\frac{\partial \bar{u}}{\partial t} \approx & -\frac{\pi^2}{4}\frac{\bar{u}}{\eta^2} + \frac{\pi^2}{12}\left[Gr(g_x + g_n\eta_x) + We\,\eta_{xxx}\right] \\
& - Re\left[1.5041\,\bar{u}\frac{\partial \bar{u}}{\partial x} + 0.1483\frac{\bar{u}}{\eta}\bar{u}\eta_x\right] \\
& + \left[4.0930\frac{\partial^2 \bar{u}}{\partial x^2} + 4.8333\frac{\eta_x}{\eta}\frac{\partial \bar{u}}{\partial x} + \left(0.1061\frac{\eta_x^2}{\eta^2} - 0.5834\frac{\eta_{xx}}{\eta}\right)\bar{u}\right]; \qquad (68)
\end{aligned}
$$

but for further comparison with falling films, in this simple situation of two-dimensional flow on a flat substrate, we also compute the next higher-order terms in the Reynolds number (which agree with Roberts 1996) to be

$$
\begin{aligned}
& + \frac{Gr\,g_x\,Re}{100}[0.7985\,\eta^2\bar{u}_x + 2.527\,\eta\eta_x\bar{u}] \\
& + \frac{Re^2}{100}\left[0.118\,\eta^2\bar{u}\bar{u}_x^2 + 0.783\,\eta^2\bar{u}^2\bar{u}_{xx} + 0.044\,\eta\eta_x\bar{u}^2\bar{u}_x\right. \\
& \quad \left. - 1.88\,\eta_x^2\bar{u}^3 - 1.03\,\eta\eta_{xx}\bar{u}^3\right]. \qquad (69)
\end{aligned}
$$

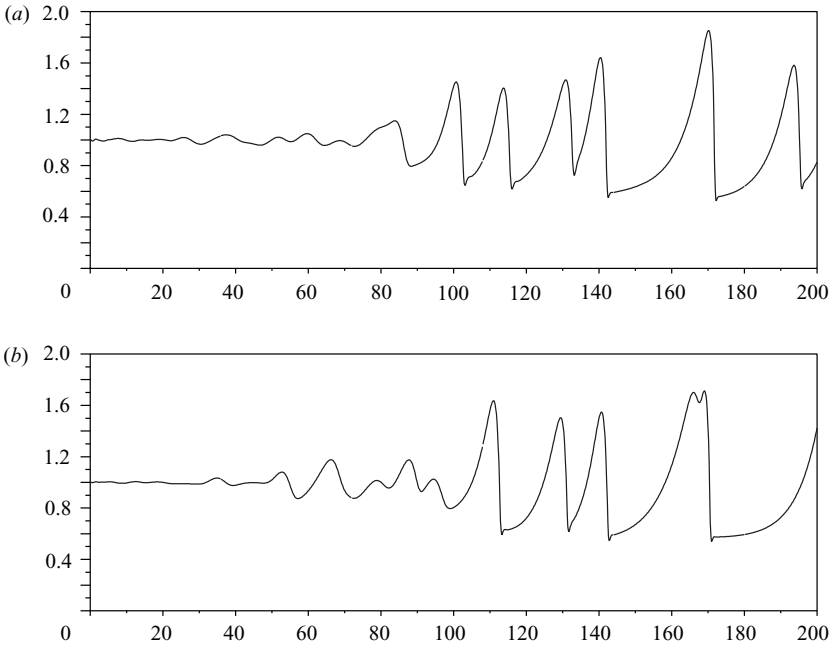

FIGURE 6. Two instants of a two-dimensional fluid falling down a vertical plane substrate with Reynolds number $Re = 20$, gravity and Weber number $Gr = We = 3$. The fluid thickness η as a function of distance x shows that white noise at the inlet $x = 0$ is selectively amplified to solitary pulses that move and merge: the close pair of pulses near $x \approx 130$ in (a) at time $t = 145$, move and merge to the large pulse at $x \approx 165$ in (b) at time $t = 160$.

Wave transitions. The model (67)–(68) resolves one-dimensional wave transitions such as those reported by Ramaswarmy, Chippada & Joo (1996), Vlachogiannis & Bontozoglou (2001) and Chang *et al.* (2002). The parabolicized Navier–Stokes equation (1) of Chang *et al.* (2002) corresponds to our non-dimensional Navier–Stokes equation (23) with $Gr = We = 3$ and our Reynolds number $Re = 15\delta$ for Chang *et al.*'s parameter δ. See in figure 6 the corresponding simulations of our model (67)–(68) restricted to two-dimensional flow (as in Roberts 1996) and forced by small white noise at the inlet (the noise is superimposed upon plane parallel Nusselt flow). The forcing here is a little larger than that of Chang *et al.* (2002), but the evolution and merger of the solitary pulses are qualitatively the same; the only noticeable difference is that the retained second-order viscous dissipation in our modelling almost entirely removes the surface tension waves in front of the solitary pulses.

For a quantitative comparison, we look at the linear stability of the Nusselt flow down an inclined plane. Adopt the non-dimensionalization of Ruyer-Quil & Manneville (1998) to compare with their results: set $Re = Gr = g_x = 1$, $g_n = B$, $We = Wh_0^2$ and consider the stability of the uniform Nusselt flow with fluid thickness $\eta = h_0$ and mean velocity $\bar{u} = h_0^2/3$. Seeking perturbations proportional to $\exp(\mathrm{i}kx/h_0 + \lambda t)$, asymptotic analysis of our model (67)–(68) for small non-dimensional wavenumber k leads to growth rates

$$\frac{\lambda}{h_0} = -\mathrm{i}k + k^2(0.3841R - 0.3333B) + \mathrm{i}k^3(1.027 + 0.5443R^2 - 0.4723BR) + k^4(-2.092R - 0.9506R^3 - 0.3333W + 0.5529B + 0.9805BR^2 - 0.1351B^2R) + O(k^5), \tag{70}$$

in terms of a different Reynolds number $R = h_0^3/3$: the imaginary terms in ik and ik^3 determine the wave speed of perturbations; the real terms in k^2 and k^4 determine their stability. Compare this with the exact asymptotic results of the Orr–Sommerfeld equation (Ruyer-Quil & Manneville 1998, equation (88))

$$\frac{\lambda}{h_0} = -ik + k^2(0.4R - 0.3333B) + ik^3(1 + 0.5714R^2 - 0.4762BR) + k^4(-2.103R - 1.011R^3 - 0.3333W + 0.6B + 1.002BR^2 - 0.1333B^2R) + O(k^5). \tag{71}$$

Our model has all the relevant dependencies upon the physical parameters, which improves on the first-order model of Ruyer-Quil & Manneville (1998). The values of the coefficients are slightly different in (70) and (71): for example, the onset of roll wave instability, controlled by the k^2 term, is slightly altered by a difference of 4% in the coefficient of the Reynolds-number R dependence. However, conversely, the decay of parallel shear flow to the Nusselt flow is at exactly the correct rate of $-\pi^2/(4h_0^2)$ for our model (68), whereas the first-order and second-order simplified model of Ruyer-Quil & Manneville (2000) has a slightly incorrect decay rate of $-5/(2h_0^2)$, an error of 1.3%. Further, the coefficients in our asymptotic growth rates (70) are largely corrected by including the higher-order terms (69) originally derived by Roberts (1996); these stability predictions would then be comparable to the second-order model (78)–(80) of Ruyer-Quil & Manneville (1998). We do not proceed here to seek higher-order accuracy obtainable with the terms (69) because our emphasis is on the complex models required to cater for three-dimensional flow over complex substrate curvatures rather than the relatively simple two-dimensional falling film.

Solitary waves. Ruyer-Quil & Manneville (2000) explored the solitary waves predicted by various thin-film models. One wide-ranging comparison was of the solitary waves falling down a vertical plate on different thicknesses of fluid. The solitary wave speeds and the peak solitary wave heights are a function of a Reynolds number $R = h_0^2/3$ where h_0 is the non-dimensional upstream and downstream film thickness. Figure 7 plots the predictions for our model (67)–(68) and our higher-order model (67)–(69) compared to three other models taken from figure 2 of Ruyer-Quil & Manneville (2000). (The agreement between the circle points digitized from figure 2 of Ruyer-Quil & Manneville (2000) and the underlying curve computed by us using their model (41) confirms that our numerical scheme is reasonably accurate.) The overall trends agree between the four models: the quantitative agreement between our higher-order model and that of Ruyer-Quil & Manneville (2000) is good up to about $R = 2.3$, but for larger R, the models are all a little different. We have no indications about which is the most accurate for larger R. In particular, the moderate agreement between our model and Shkadov's integral boundary layer model (Ruyer-Quil & Manneville 2000, equations (2)–(3)) is probably fortuitous owing to Shkadov's higher bed drag ameliorating the lack of 'Trouton' viscosity that we resolve: Shkadov's solitary waves have more extensive oscillatory ripples than we predict.

Three-dimensional-instabilities. Three-dimensional instabilities of waves flowing down a vertical plate occur in at least two different forms (Liu, Schneider & Gollub 1995). Consider our model (65)–(66) of three-dimensional flow with periodic boundary conditions in the two horizontal dimensions of the flat substrate. Numerical evolution of the model (65)–(66) plotted in figure 8 shows the growth of a nearly synchronous instability (spanwise deformations of adjacent wave fronts have nearly the same

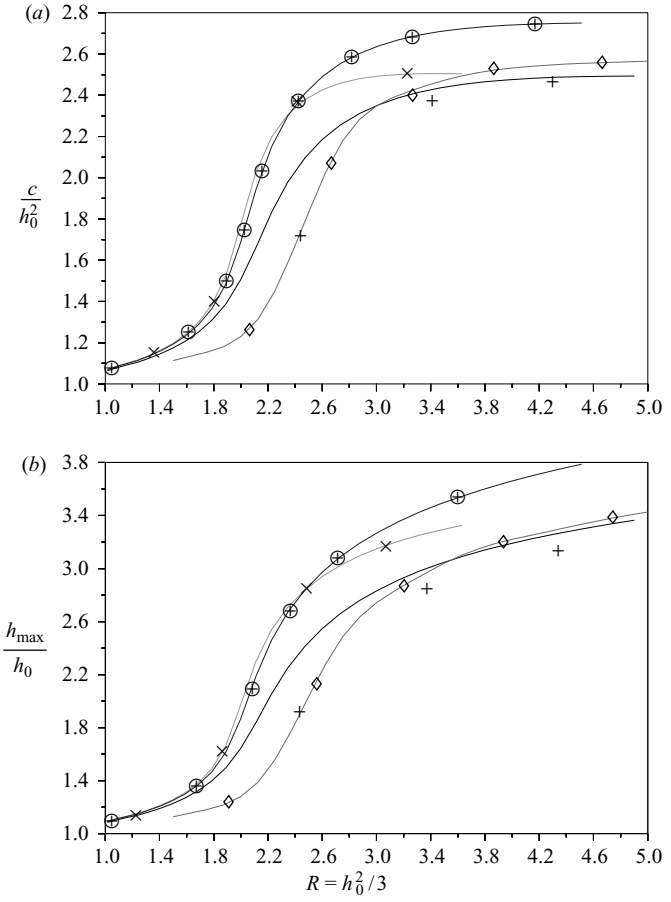

FIGURE 7. (*a*) Solitary wave speed c, and (*b*) solitary wave peak height h_{max} as a function of a Reynolds number R on vertically falling films of different non-dimensional thicknesses h_0: the plain curve is from our model (67)–(68); the curve (our computations) with circles is the simplified second-order model (41) from Ruyer-Quil & Manneville (2000) (digitized from figure 2); the curve with crosses is our higher-order model (67)–(69); the curve with diamonds is the Shkadov model (Ruyer-Quil & Manneville 2000, equations (2)–(3)); and the plus points (also digitized) are the results of Chang, Demekhin & Kopelevich (1993). Parameters are $Re = Gr = g_x = 1$, $g_n = 0$ and $We = 252$ to match.

transverse phase), which not only affects the wave shape but also has a marked effect on the depth of the trough, as noted in the experiments of Liu *et al.* (1995).

Faraday waves. Vigorous vertical vibration of a layer of fluid on a flat plate leads to a rich repertoire of spatio-temporal dynamics (e.g. Miles & Henderson 1990; Perlin & Schultz 2000; Burya & Shkadov 2001), such as those shown in figure 9. Using our model (65)–(66) of three-dimensional flow, with periodic boundary conditions in the two horizontal dimensions, we choose the reference velocity to be the shallow-water wave speed $U = \sqrt{gH}$ then the non-dimensional parameters $Re = Gr$. Achieve the vertical vibration simply by modulating the normal gravity in (65)–(66) by, for example, the factor $1 + 0.55\sin(2.2\,t)$. This frequency is roughly twice that of waves with wavelength 5 and see in figure 9 that these waves are generated by a Mathieu-like

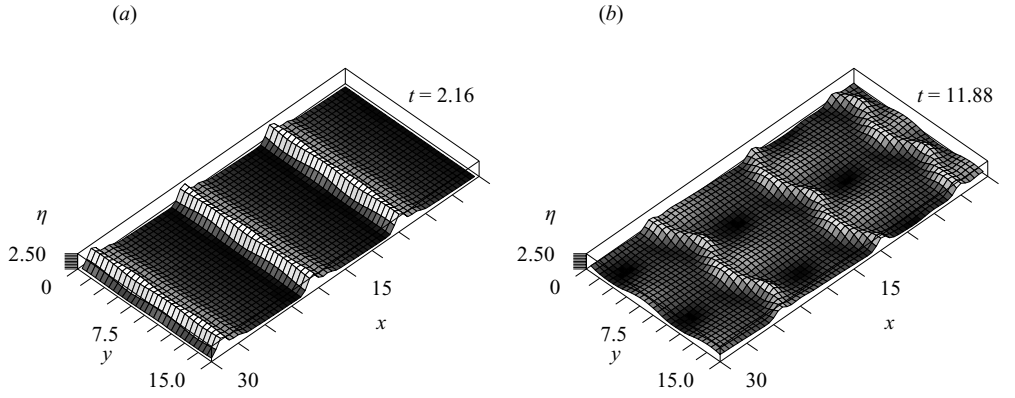

FIGURE 8. (*a*) Roll waves on the fluid flowing down a vertical plate exhibit (*b*) the three-dimensional synchronous instability to break up the simple pattern: for mean fluid thickness 1, $Re = 20$, $Gr = We = 3$.

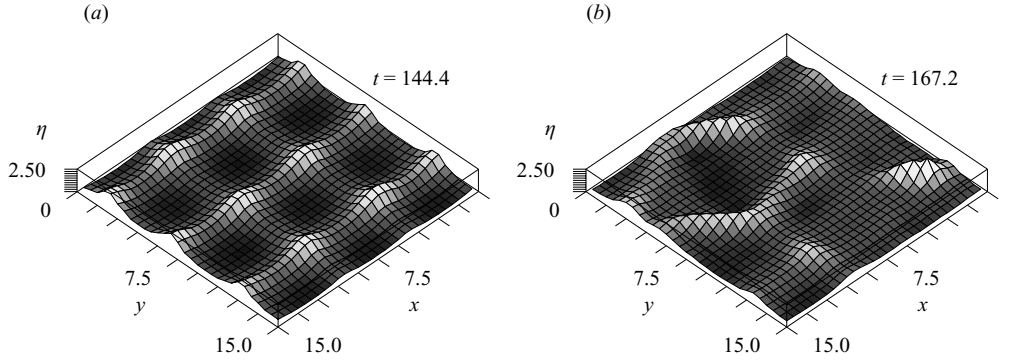

FIGURE 9. Two instants of unsteady waves on a vertically vibrating flat plate simulating the Faraday waves vacillating between (*a*) ordered patterns and (*b*) irregular patterns: for mean fluid thickness 1, no surface tension, $Re = Gr = 40$, and normal gravity modulated by the factor $1 + 0.55\sin(2.2\,t)$.

instability. However, involved nonlinear interactions lead to complex evolution of the spatial pattern of waves, as is well known in experiments.

Vorticity and divergence. Consider the linearized dynamics of small variations on a film of nearly constant thickness when governed by the model (64)–(66): $\eta = 1 + h(x, y, t)$ where h and the lateral velocity $\bar{\boldsymbol{u}}$ are small. The linearized versions of (64)–(66) are

$$\begin{aligned} h_t &= -\bar{u}_x - \bar{v}_y, \\ Re\,\bar{u}_t &= -\frac{\pi^2}{4}\bar{u} + \frac{\pi^2}{12}[Gr(g_x + g_n h_x) + We(h_{xxx} + h_{xyy})] \\ &\quad + (1+\varpi)\bar{u}_{xx} + \bar{u}_{yy} + \varpi\,\bar{v}_{xy}, \\ Re\,\bar{v}_t &= -\frac{\pi^2}{4}\bar{v} + \frac{\pi^2}{12}[Gr(g_y + g_n h_y) + We(h_{xxy} + h_{yyy})] \\ &\quad + \bar{v}_{xx} + (1+\varpi)\bar{v}_{yy} + \varpi\,\bar{u}_{xy}, \end{aligned}$$

where $\varpi = 3.0930$ (the term ϖ is chosen because its value is coincidentally close to π).

(i) Take ∂_y of the second from ∂_x of the third to deduce equation (8) governing the mean normal vorticity $\bar{\omega} = \bar{v}_x - \bar{u}_y$. Observe that linearly it is decoupled from the other components of the fluid dynamics: the mean normal vorticity simply decays by drag on the substrate and by lateral diffusion.

(ii) Conversely, the first of the linearized equations together with the divergence of the second two equations decouple from the mean normal vorticity to give (9)–(10) for the film thickness and the mean flow divergence $\bar{\delta} = \bar{u}_x + \bar{v}_y$ as discussed briefly in § 1. A little analysis shows that in the absence of gravity ($Gr = 0$) this model predicts damped waves for lateral wavenumbers

$$a > a_c = \frac{\pi/2}{\sqrt{\pi\sqrt{Re\,We/3} - (1+\varpi)}}.$$

Numerical solutions of the physical eigenvalue problem agree closely with this for $Re\,We > 30$, even though the critical wavenumber is as large as $a_c \approx 0.65$. Recall that the limit (62) on logarithmic derivatives in this model implies the wavenumber must be less than $1.9/\eta$; here, the critical $a_c \approx 0.65$ on a fluid of depth near 1 is comfortably within the limit. Waves cannot be captured by the single mode of a lubrication model such as (1).

(iii) In this linear approximation, lateral components of gravity just induce a mean flow in the direction of the lateral component.

Substrate curvature and the nonlinear effects of advection and large-scale variations in the thickness modify this description of the basic dynamics of the fluid film.

Radial flow with axisymmetry. Turn on a tap producing a steady stream into a basin with a flat bottom; the flow spreads out in a thin layer, then at some radial distance, it undergoes a hydraulic jump to a thicker layer spreading more slowly (e.g. Bohr *et al.* 1996). A model with inertia is essential for modelling such a hydraulic jump. Here, use polar coordinates (r, θ), whence the substrate has zero curvature $k_1 = k_2 = 0$, but scale factors $m_1 = 1$ and $m_2 = r$. Then describe axisymmetric dynamics by neglecting angular flow and variations while retaining the radial velocity $\bar{u}$ in our three-dimensional flow model (64)–(66):

$$\begin{aligned}
\eta_t &= -\frac{1}{r}\partial_r(r\bar{u}\eta),\\
Re\,\bar{u}_t &= -\frac{\pi^2}{4}\frac{\bar{u}}{\eta^2} + 1.4167\frac{\eta_r}{r\eta}\bar{u} + \frac{\pi^2}{12}\left[Gr\,g_n\eta_r + We\,\partial_r\left\{\frac{1}{r}\partial_r(r\eta_r)\right\}\right]\\
&\quad - Re\left[1.5041\,\bar{u}\bar{u}_r + 0.1577\frac{1}{r}\bar{u}^2 + 0.1483\frac{\eta_r}{\eta}\bar{u}^2\right]\\
&\quad + \left[4.0930\,\partial_r\left\{\frac{1}{r}\partial_r(r\bar{u})\right\} + 4.8333\frac{\eta_r}{\eta}\bar{u}_r + \left(0.1061\frac{\eta_r^2}{\eta^2} - 0.5834\frac{\eta_{rr}}{\eta^2}\right)\bar{u}\right].
\end{aligned}$$

The above equations may be integrated in time to see evolving dynamics in a radial flow in a similar manner to the solutions just discussed. However, here we focus on steady flow and so adopt Newton iteration to find solutions. We fix the inlet condition of flow leaving the tap with prescribed thickness and velocity (in figure 10 the flow has $\eta = 2.25$ and $\bar{u} = 2.62$ at radius $r = 5$) and exiting the domain with some prescribed mean velocity at large distance ($\bar{u} = 0.16$ at $r = 50$ in figure 10). Newton iteration then finds the steady solutions for fluid thickness $\eta(r)$ and mean velocity $\bar{u}(r)$ shown in figure 10(*a*). The flow spreads out in a supercritical thin ($\eta \approx 1$) fast flow before

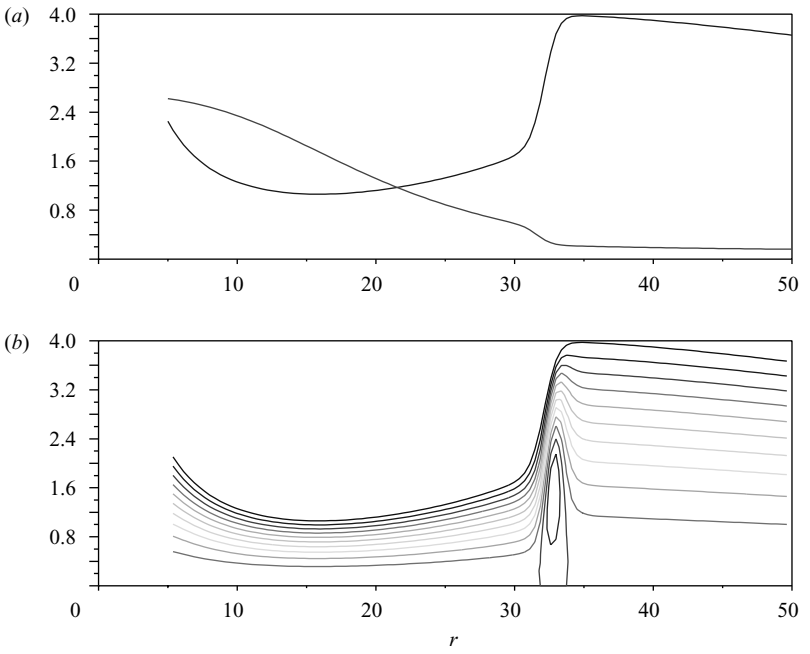

FIGURE 10. Steady axisymmetric radial flow on a flat substrate: (*a*) free-surface thickness η and mean velocity $\bar{u}$ versus radius r; (*b*) streamlines showing a recirculation under the hydraulic jump at $r \approx 33$. The Reynolds number $Re = 15$, gravity number $Gr = 1$ and no surface tension, $We = 0$.

undergoing a hydraulic jump at distance $r \approx 33$ to a subcritical thick ($\eta \approx 4$) slow flow. The streamlines in figure 10(*b*), obtained from the velocity fields (51)–(52), show the presence of a recirculation under the jump, as also seen in the experiments by Bohr *et al.* (1996), see also Watanabe, Putkaradze & Bohr (2003). Our model expressed in depth-averaged quantities resolves such non-trivial internal flow structures.

The steady flow in figure 10 is near the limit of applicability of the model. Although the free surface looks steep in the figure, the slope is everywhere less than 1.08 which, although less than the limit (62) identified earlier, is about as large as we could reasonably use. For interest, other lateral derivatives have the following ranges: $\eta_{rr} \in [-0.88, 0.74]$, $\bar{u}_r \in [-0.15, 0]$ and $\bar{u}_{rr} \in [-0.08, 0.11]$. We also find the hydraulic jump with recirculation in less extreme flows than that shown in figure 10. However, we have not yet found any flows with an extra eddy at the surface of the hydraulic jump, as reported for experiments with larger jumps (discussed by Watanabe *et al.* 2003, § 2.1).

6.2. *Flow outside a cylinder resolves evolving beads*

Thin-film flows on the outside or inside of circular cylinders or tubes are important in a number of biological and engineering applications. For example, Jensen (1997) studied the effects of surface tension on a thin liquid layer lining the interior of a cylindrical and curving tube and derived a corresponding evolution equation in the lubrication approximation. Our model (57)–(58) could be used to extend his modelling to flows with inertia. Similarly, Atherton & Homsy (1976), Kalliadasis & Chang (1994) and Kliakhandler *et al.* (2001) considered coating flow down vertical fibres and similarly derived nonlinear lubrication models. Alekseenko *et al.* (1996) observed the instabilities of rivulet flow underneath a sloping cylinder and called for

an appropriate theoretical model. Here we record the model (57)–(58) as it appears in full for flows both inside and outside a circular cylinder. The specific model for a circular tube which is bent and twisted is left for later work.

Use a coordinate system with s the axial coordinate and θ the angular coordinate; denote the averaged axial and angular velocities by $\bar{\boldsymbol{u}}$ with components $\bar{u}$ and $\bar{v}$, respectively. The substrate has scale factors $m_1 = 1$ and $m_2 = R$, where R is the radius of the cylinder, and curvatures $k_1 = 0$ and $k_2 = \mp 1/R$, where the upper/lower sign is for flow outside/inside of the cylinder. Then the model on a cylinder is, where here $\zeta = \eta \pm \eta^2/(2R)$,

$$\frac{\partial \zeta}{\partial t} \approx -\frac{\partial(\eta \bar{u})}{\partial s} - \frac{1}{R}\frac{\partial(\eta \bar{v})}{\partial \theta}, \tag{72}$$

$$\begin{aligned}
Re\,\frac{\partial \bar{u}}{\partial t} \approx\ & -\frac{\pi^2}{4}\frac{\bar{u}}{\eta^2} \pm \frac{\bar{u}}{R\eta} - 0.6487\frac{\bar{u}}{R^2} + We\,\frac{\pi^2}{12}\left[\frac{1}{R^2}\eta_s + \eta_{sss} + \frac{1}{R^2}\eta_{s\theta\theta}\right] \\
& + Gr\left[\frac{\pi^2}{12}(g_s + g_n\eta_s) \pm 0.4891\frac{g_s\eta}{R}\right] \\
& - Re\left[1.5041\,\bar{u}\frac{\partial \bar{u}}{\partial s} + 1.3464\frac{\bar{v}}{R}\frac{\partial \bar{u}}{\partial \theta} + 0.1577\frac{\bar{u}}{R}\frac{\partial \bar{v}}{\partial \theta} + 0.1483\frac{\bar{u}}{\eta}\left(\bar{u}\eta_s + \frac{\bar{v}}{R}\eta_\theta\right)\right] \\
& + \left[4.0930\frac{\partial^2 \bar{u}}{\partial s^2} + \frac{1}{R^2}\frac{\partial^2 \bar{u}}{\partial \theta^2} + 3.0930\frac{1}{R}\frac{\partial^2 \bar{v}}{\partial s\,\partial \theta}\right. \\
& \quad + 4.8333\frac{\eta_s}{\eta}\frac{\partial \bar{u}}{\partial s} + \frac{\eta_\theta}{R^2\eta}\frac{\partial \bar{u}}{\partial \theta} + 1.9167\frac{\eta_s}{R\eta}\frac{\partial \bar{v}}{\partial \theta} + 1.9167\frac{\eta_\theta}{R\eta}\frac{\partial \bar{v}}{\partial s} \\
& \quad + \left(-0.5033\frac{\eta_\theta^2}{R^2\eta^2} - \frac{\eta_{\theta\theta}}{2R^2\eta} + 0.1061\frac{\eta_s^2}{\eta^2} - 0.5834\frac{\eta_{ss}}{\eta}\right)\bar{u} \\
& \quad \left. + \left(0.6094\frac{\eta_\theta\eta_s}{R\eta^2} - 0.0833\frac{\eta_{s\theta}}{R\eta}\right)\bar{v}\right],
\end{aligned} \tag{73}$$

$$\begin{aligned}
Re\,\frac{\partial \bar{v}}{\partial t} \approx\ & -\frac{\pi^2}{4}\frac{\bar{v}}{\eta^2} \pm \frac{3\bar{v}}{R\eta} - 2.8381\frac{\bar{v}}{R^2} + We\,\frac{\pi^2}{12}\left[\frac{1}{R^2}\frac{\eta_\theta}{R} + \frac{1}{R}\eta_{ss\theta} + \frac{1}{R^3}\eta_{\theta\theta\theta}\right] \\
& + Gr\left[\frac{\pi^2}{12}\left(g_\theta + g_n\frac{\eta_\theta}{R}\right) \pm 0.2337\frac{g_\theta\eta}{R}\right] \\
& - Re\left[1.3464\,\bar{u}\frac{\partial \bar{v}}{\partial s} + 1.5041\frac{\bar{v}}{R}\frac{\partial \bar{v}}{\partial \theta} + 0.1577\,\bar{v}\frac{\partial \bar{u}}{\partial s} + 0.1483\frac{\bar{v}}{\eta}\left(\bar{u}\eta_s + \frac{\bar{v}}{R}\eta_\theta\right)\right] \\
& + \left[\frac{\partial^2 \bar{v}}{\partial s^2} + 4.0930\frac{1}{R^2}\frac{\partial^2 \bar{v}}{\partial \theta^2} + 3.0930\frac{1}{R}\frac{\partial^2 \bar{u}}{\partial s\,\partial \theta} + 4.8333\frac{\eta_\theta}{R^2\eta}\frac{\partial \bar{v}}{\partial \theta} + \frac{\eta_s}{\eta}\frac{\partial \bar{v}}{\partial s}\right. \\
& \quad + 1.9167\frac{\eta_s}{R\eta}\frac{\partial \bar{u}}{\partial \theta} + 1.9167\frac{\eta_\theta}{R\eta}\frac{\partial \bar{u}}{\partial s} + \left(-0.5033\frac{\eta_s^2}{\eta^2} - \frac{\eta_{ss}}{2\eta} + 0.1061\frac{\eta_\theta^2}{R^2\eta^2}\right. \\
& \quad \left.\left. - 0.5834\frac{\eta_{\theta\theta}}{R^2\eta}\right)\bar{v} + \left(0.6094\frac{\eta_\theta\eta_s}{R\eta^2} - 0.0833\frac{\eta_{s\theta}}{R\eta}\right)\bar{u}\right],
\end{aligned} \tag{74}$$

For a non-trivial example, see the beading of fluid on a thin fibre in figures 1 and 2 (from solutions using periodic boundary conditions along the cylinder): vertical gravity first rather quickly moves a lump of fluid to below the nearly horizontal cylinder of the fibre (gravity number $Gr = 0.5$ in the figures); thereafter, surface tension more slowly gathers more fluid into the beading fluid which beads mainly below, but also above the fibre (Weber number $We = 20$ in the figures); gravity causes the

fluid bead to stabilize off the centre of the fibre (curiously, there is more in the bead above the fibre than in the original lump); and finally the bead slides along the fibre as it is angled downward a little. The three time scales in this evolution, the fast gravity forced flow, the slower surface-tension-driven flow, and the even longer-term sliding, are captured in our model.

Obtain axisymmetric flows by setting to zero any derivatives with respect to θ, and also setting $g_n = g_\theta = 0$ as non-zero values would break the symmetry. The equation for $\bar{v}$ then just describes the decay of angular flow around the cylinder, so also set $\bar{v} = 0$. Thus, the axisymmetric model is

$$\frac{\partial \zeta}{\partial t} \approx -\frac{\partial(\eta \bar{u})}{\partial s}, \tag{75}$$

$$\begin{aligned} Re\,\frac{\partial \bar{u}}{\partial t} \approx & -\frac{\pi^2}{4}\frac{\bar{u}}{\eta^2} \pm \frac{\bar{u}}{R\eta} - 0.6487\frac{\bar{u}}{R^2} + We\,\frac{\pi^2}{12}\left[\frac{1}{R^2}\eta_s + \eta_{sss}\right] \\ & + Gr\left[\frac{\pi^2}{12}g_s \pm 0.4891\frac{g_s\eta}{R}\right] \\ & - Re\left[1.5041\,\bar{u}\frac{\partial \bar{u}}{\partial s} + 0.1483\frac{\bar{u}}{\eta}\bar{u}\frac{\partial \eta}{\partial s}\right] + \left[4.0930\frac{\partial^2 \bar{u}}{\partial s^2}\right. \\ & \left. + 4.8333\frac{\eta_s}{\eta}\frac{\partial \bar{u}}{\partial s} + \left(0.1061\frac{\eta_s^2}{\eta^2} - 0.5834\frac{\eta_{ss}}{\eta}\right)\bar{u}\right]; \end{aligned} \tag{76}$$

recall that the upper/lower sign is for flow outside/inside of the cylinder. As in lubrication models (Roy *et al.* 2002, p. 254), see that surface tension in the cylindrical geometry acts through the term $We\,\eta_s/R^2$ in (76) or (73) rather like a radially outward body force such as the term $Gr\,g_n\eta_s$ in (73).

Now consider the stability to axisymmetric disturbances of a uniform layer of fluid flowing down a cylindrical fibre. Choose the velocity scale so that $Gr = 1$ to match the experiments and analysis of Kliakhandler *et al.* (2001). Upon a cylinder of non-dimensional radius $R = 2$, relative to the fluid thickness, the equilibrium mean fluid velocity down the cylinder is predicted to be $\bar{u} = 0.501$; seeking disturbance proportional to $\exp(\mathrm{i}kx + \lambda t)$ in (75)–(76), we find the asymptotic expression for the growth rate

$$\begin{aligned} \lambda = & -1.106\,\mathrm{i}k + k^2(0.06437\,We + 0.1162\,Re) + \mathrm{i}k^3(1.393 \\ & + 0.034\,Re\,We + 0.06136\,Re^2) + k^4(-0.3812\,We - 0.9588\,Re \\ & - 0.001946\,Re\,We^2 - 0.02498\,Re^2\,We - 0.03875\,Re^3) + O(k^5). \end{aligned} \tag{77}$$

For the very slow flow case presented by Kliakhandler *et al.* (2001), $Re = 0$, we predict a growth rate $\mathrm{Re}(\lambda) = We\,k^2(0.06437 - 0.3812\,k^2)$ which gives the unstable band of wavenumbers as $|k| < 0.41$. This matches reasonably the numerically exact band of $|k| < 0.33$ shown in figure 3(*b*) of Kliakhandler *et al.* (2001), given the significant substrate curvature $\kappa = 1/R = 1/2$ of this cylinder.

6.3. *Flow about a small channel grows vortices*

Consider the flow on a substrate with a small channel aligned downhill. We compare this viscous flow with the high-Reynolds-number experiments of Bousmar (2002) and Bousmar & Zech (2003) who modelled turbulent flow over flood plains and channels in a flume with water of variable depth, but of the order of 5 cm deep.

First, create the coordinate system. Bousmar's channel and flood plain had constant shape along the stream, the depth varied only across the stream. Thus, here let $s = x_1$

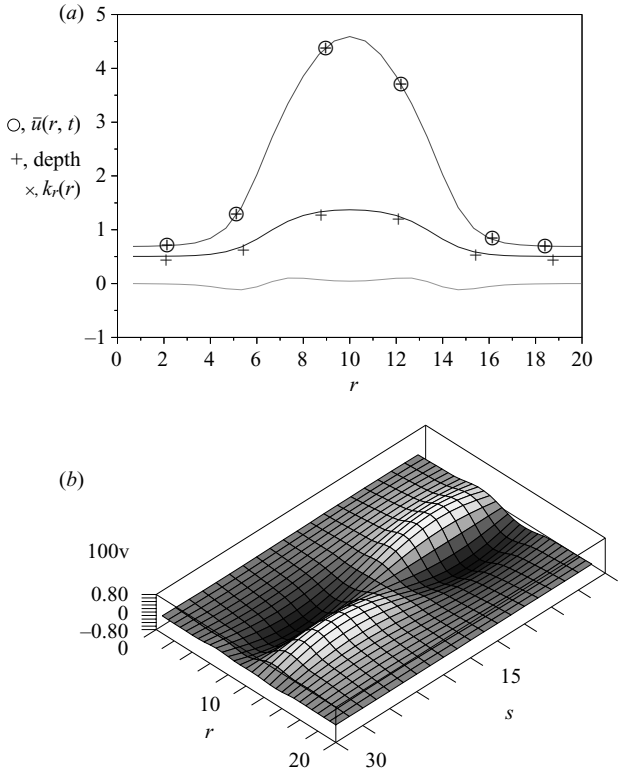

FIGURE 11. (*a*) An example channel is three times as deep in the middle as the surrounding shallows; the substrate has curvature k_r; and the fluid flow is eight times as fast in the channel as in the shallows; (*b*) this base flow is unstable to superimposed travelling vortices on the shear near the sides of the channel as shown by the cross-channel velocity. Here, $Re = Gr = 80$ on a substrate at angle $\vartheta = 0.1$ rad, with $We = 0$.

be the along stream coordinate, and $r = x_2$ be the horizontal distance across the stream on the substrate. (There is no good reason for using the variable name r for distance horizontally across the stream, only that it is next to the letter s in the alphabet. In this subsection the variable r is not used to indicate any sort of radius.) The curved substrate is located a distance $d(r) > 0$ from the (s, r)-plane in a normal direction, that is the substrate position $\boldsymbol{P}(s, r) = r\boldsymbol{i} - d(r)\boldsymbol{j} + s\boldsymbol{k}$ using $\boldsymbol{j}$, $\boldsymbol{k}$ and $\boldsymbol{i}$ as the vertical and two horizontal unit vectors, see the example $d(r)$ in the middle curve of Figure 11(*a*). Thus, the unit vectors, scale factors and curvature of the substrate coordinate system are (useful relationships are: $m_r^2 = 1 + d'^2$, $d'' = -k_r m_r^3$, and $m_r' = -d' k_r m_r^2$)

$$\boldsymbol{e}_s = \boldsymbol{k}, \quad \boldsymbol{e}_r = \frac{1}{\sqrt{1+d'^2}}(\boldsymbol{i} - d'\boldsymbol{j}), \qquad \boldsymbol{e}_n = \frac{1}{\sqrt{1+d'^2}}(d'\boldsymbol{i} + \boldsymbol{j}),$$
$$m_s = 1, \quad m_r = \sqrt{1+d'^2},$$
$$k_s = 0, \quad k_r = -\frac{d''}{(1+d'^2)^{3/2}}.$$

This expression for the curvature k_r is well known. The normal coordinate y is not the vertical coordinate, and so a flat fluid surface located at, say, the location of

the reference (s, r)-plane is represented by the varying $y = d(1 + d'^2)^{1/2}$. Similarly non-trivial, as the channel slopes down at an angle $\vartheta = 0.1$ radians to the horizontal and not sideways tilted, the gravitational forcing is in the direction

$$\hat{\boldsymbol{g}} = \sin\vartheta\, \boldsymbol{e}_s + \frac{d'}{m_r}\cos\vartheta\, \boldsymbol{e}_r - \frac{1}{m_r}\cos\vartheta\, \boldsymbol{e}_n. \tag{78}$$

This coordinate system suits any flow where the substrate is almost arbitrarily curved in only one direction, not just flow along a channel. (The model (79)–(81) reduces to that for the flow outside/inside a cylinder, (72)–(74), when $r = \theta$ and the substrate scale factors are set to $k_r = \mp 1/R$ and $m_r = R$ (only the direction of gravity (78) is incorrect). This algebraic connection occurs despite the cylinder not being strictly encompassed by a depth $d(r)$ below any reference plane. Indeed, the beading flow on a cylinder shown in figures 1 and 2 was actually obtained using code for the model (79)–(81) of this subsection.)

Secondly, computer algebra gives the model on this substrate as, where here $\zeta = \eta - k_r\eta^2/2$,

$$\frac{\partial\zeta}{\partial t} \approx -\frac{\partial(\eta\bar{u})}{\partial s} - \frac{1}{m_r}\frac{\partial(\eta\bar{v})}{\partial r}, \tag{79}$$

$$\begin{aligned}
Re\,\frac{\partial\bar{u}}{\partial t} \approx{}& -\frac{\pi^2}{4}\frac{\bar{u}}{\eta^2} - k_r\frac{\bar{u}}{\eta} - 0.6487\,k_r^2\bar{u} + We\,\frac{\pi^2}{12}\left[k_r^2\eta_s + \eta_{sss} + \frac{1}{m_r}\frac{\partial}{\partial r}\left(\frac{1}{m_r}\frac{\partial\eta_s}{\partial r}\right)\right] \\
&+ Gr\left[\frac{\pi^2}{12}(g_s + g_n\eta_s) - 0.4891\,k_r g_s\eta\right] \\
&- Re\left[1.5041\,\bar{u}\frac{\partial\bar{u}}{\partial s} + 1.3464\frac{\bar{v}}{m_r}\frac{\partial\bar{u}}{\partial r} + 0.1577\frac{\bar{u}}{m_r}\frac{\partial\bar{v}}{\partial r}\right. \\
&\qquad \left. + 0.1483\frac{\bar{u}}{\eta}\left(\bar{u}\eta_s + \frac{\bar{v}}{m_r}\eta_r\right)\right] \\
&+ \left[4.0930\frac{\partial^2\bar{u}}{\partial s^2} + \frac{1}{m_r}\frac{\partial}{\partial r}\left(\frac{1}{m_r}\frac{\partial\bar{u}}{\partial r}\right) + 3.0930\frac{1}{m_r}\frac{\partial^2\bar{v}}{\partial s\partial r}\right. \\
&\quad + 4.8333\frac{\eta_s}{\eta}\frac{\partial\bar{u}}{\partial s} + \frac{\eta_r}{m_r^2\eta}\frac{\partial\bar{u}}{\partial r} + 1.9167\frac{\eta_s}{m_r\eta}\frac{\partial\bar{v}}{\partial r} + 1.9167\frac{\eta_r}{m_r\eta}\frac{\partial\bar{v}}{\partial s} \\
&\quad + \left(-0.5033\frac{\eta_r^2}{m_r^2\eta^2} - \frac{1}{2\eta m_r}\frac{\partial}{\partial r}\left(\frac{\eta_r}{m_r}\right) + 0.1061\frac{\eta_s^2}{\eta^2} - 0.5834\frac{\eta_{ss}}{\eta}\right)\bar{u} \\
&\quad \left. + \left(0.6094\frac{\eta_r\eta_s}{m_r\eta^2} - 0.0833\frac{\eta_{sr}}{m_r\eta}\right)\bar{v}\right],
\end{aligned} \tag{80}$$

$$\begin{aligned}
Re\,\frac{\partial\bar{v}}{\partial t} \approx{}& -\frac{\pi^2}{4}\frac{\bar{v}}{\eta^2} - k_r\frac{3\bar{v}}{\eta} - 2.8381\,k_r^2\bar{v} + We\,\frac{\pi^2}{12}\left[\frac{k_r'}{m_r} + k_r^2\frac{\eta_r}{m_r} + \frac{\eta_{ssr}}{m_r}\right. \\
&\qquad \left. + \frac{1}{m_r}\frac{\partial}{\partial r}\left(\frac{1}{m_r}\frac{\partial}{\partial r}\left\{\frac{\eta_r}{m_r}\right\}\right) + 2.7159\,\frac{\eta k_r k_r'}{m_r}\right] \\
&+ Gr\left[\frac{\pi^2}{12}\left(g_r + g_n\frac{\eta_r}{m_r}\right) - 0.2337\,k_r g_r\eta\right] \\
&- Re\left[1.3464\,\bar{u}\frac{\partial\bar{v}}{\partial s} + 1.5041\frac{\bar{v}}{m_r}\frac{\partial\bar{v}}{\partial r} + 0.1577\,\bar{v}\frac{\partial\bar{u}}{\partial s}\right.
\end{aligned}$$

$$+0.1483\frac{\bar{v}}{\eta}\left(\bar{u}\eta_s+\frac{\bar{v}}{m_r}\eta_r\right)\Bigg]$$
$$+\Bigg[\frac{\partial^2\bar{v}}{\partial s^2}+4.0930\frac{1}{m_r}\frac{\partial}{\partial r}\left(\frac{1}{m_r}\frac{\partial\bar{v}}{\partial r}\right)+3.0930\frac{1}{m_r}\frac{\partial^2\bar{u}}{\partial s\partial r}$$
$$+4.8333\frac{\eta_r}{m_r^2\eta}\frac{\partial\bar{v}}{\partial r}+\frac{\eta_s}{\eta}\frac{\partial\bar{v}}{\partial s}+1.9167\frac{\eta_s}{m_r\eta}\frac{\partial\bar{u}}{\partial r}+1.9167\frac{\eta_r}{m_r\eta}\frac{\partial\bar{u}}{\partial s}$$
$$+\left(-0.5033\frac{\eta_s^2}{\eta^2}-\frac{\eta_{ss}}{2\eta}+0.1061\frac{\eta_r^2}{m_r^2\eta^2}-0.5834\frac{1}{\eta m_r}\frac{\partial}{\partial r}\left(\frac{\eta_r}{m_r}\right)\right)\bar{v}$$
$$+\left(0.6094\frac{\eta_r\eta_s}{m_r\eta^2}-0.0833\frac{\eta_{sr}}{m_r\eta}\right)\bar{u}\Bigg], \tag{81}$$

Lastly, as expected, simulations (with periodic boundary conditions in both lateral dimensions for both the flow and the substrate) show that fast flow develops in the deeper channel and slow flow on the shallow regions, see figure 11(*a*). However, the shear in the mean downstream velocity (figure 11*a*) is unstable to relatively weak horizontal vortices that grow in the shear and travel downstream, see them in the mean lateral velocity shown in figure 11(*b*);† analogous notable vortices were observed by Bousmar (2002) and Bousmar & Zech (2003) in their turbulent flows. As also noted by Bousmar, see that the vortices here similarly extend into the shallows, albeit weakly.

The simulation reported here has a change in depth of the substrate sufficiently big so that the nonlinear nature of the derived model is certainly essential: (Decré & Baret 2003, p. 155), comment that nonlinear theories are required in viscous flow if the change in substrate profile is larger than half the shallow fluid depth; here the factor is about three, that is, six times the linear limit identified by Decré & Baret (2003).

Stokes flow across topography is obtained by tilting this channel substrate in the r direction instead of the s direction. Mazouchi & Homsy (2001) numerically solved for the two-dimensional Stokes flow, $Re = 0$, across a step down and step up which, for significant surface tension $We > 5$, exhibited damped upstream capillary waves. See in figure 12 that our model (79)–(81), with periodic boundary conditions in lateral position r, predicts exactly the same sort of phenomena in the same parameter regime. The main difference is that we require the substrate to be a smooth base for the local coordinate system and so do not cater for the sharp changes in substrate used for the flows reported by Mazouchi & Homsy (2001). Consequently, our upstream capillary waves in figure 12 are not as large as theirs.

6.4. *Flow on the outside of a sphere*

For flow on the outside of a sphere we use a coordinate system with θ the co-latitude coordinate, ϕ the azimuthal (longitude) coordinate, and co-latitude and azimuthal velocity components $\bar{u}$ and $\bar{v}$, respectively. The substrate has scale factors $m_1 = R$ and $m_2 = R\sin\theta$ where R is the radius of the sphere, and curvatures $k_1 = k_2 = -1/R$.

† The vortices apparent in figure 11(*b*) fill the computational domain and thus may possibly be an artifice of the domain size. However, otherwise identical simulations on twice the channel length show twice as many vortices, whereas simulations in a domain half as long again show a rich modulation among vortices of roughly the shown length. We deduce that the displayed vortices are not solely an artifice of the computational domain.

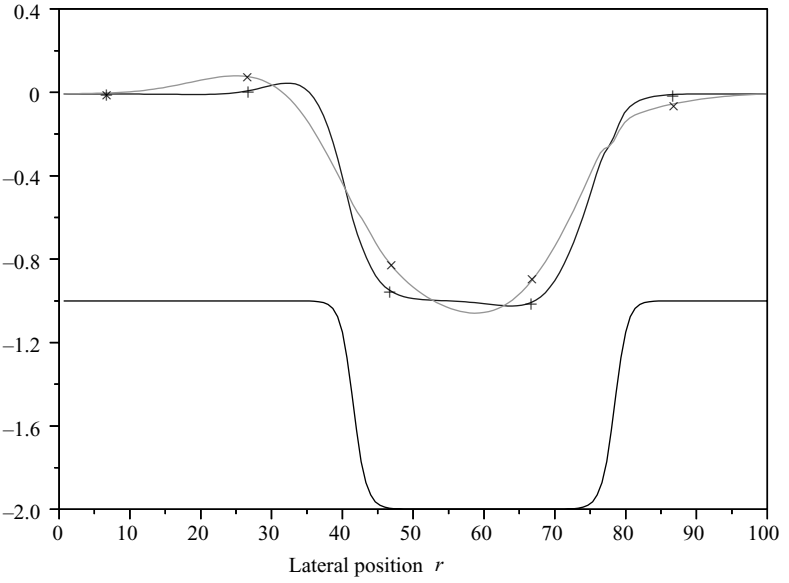

FIGURE 12. Fluid film thickness for two Weber numbers $We = 10$ (+) and 100 (×) for flow to the right over the shown substrate with a smoothed step-down and a smoothed step-up, as predicted by model (79)–(81): for near Stokes flow, $Re = 0.1$; scaled to the gravitational forcing $Gr = 1$; on a substrate at an angle $\theta = 0.2$ rad to the horizontal.

On a sphere, every point is an umbilical point; nonetheless, the earlier analysis is valid in this conventional spherical coordinate system. Then the model on a sphere is, where here $\zeta = \eta + \eta^2/R + \eta^3/(3R^2)$,

$$\frac{\partial \zeta}{\partial t} \approx -\frac{1}{R}\frac{\partial(\eta\bar{u})}{\partial\theta} - \frac{1}{R\sin\theta}\frac{\partial(\cos\theta\,\eta\bar{v})}{\partial\phi}, \tag{82}$$

$$\begin{aligned}
Re\,\frac{\partial\bar{u}}{\partial t} \approx\; & -\frac{\pi^2}{4}\frac{\bar{u}}{\eta^2} - 6.4718\frac{\bar{u}}{R^2} + Gr\left[\frac{\pi^2}{12}\left(g_\theta + \frac{g_n}{R}\eta_\theta\right) + 0.7228\frac{g_\theta\eta}{R}\right] \\
& + We\,\frac{\pi^2}{12}\left[-\frac{\cos 2\theta}{R^3\sin^2\theta}\eta_\theta + \frac{1}{R^3\sin\theta}\frac{\partial}{\partial\theta}(\sin\theta\,\eta_{\theta\theta}) + \frac{\partial}{\partial\theta}\left(\frac{1}{R^3\sin^2\theta}\eta_{\phi\phi}\right)\right] \\
& - Re\left[1.5041\frac{\bar{u}}{R}\frac{\partial\bar{u}}{\partial\theta} + 1.3464\left(\frac{\bar{v}}{R\sin\theta}\frac{\partial\bar{u}}{\partial\phi} - \frac{\cos\theta}{R\sin\theta}\bar{v}^2\right)\right. \\
& \qquad \left. + 0.1577\left(\frac{\bar{u}}{R\sin\theta}\frac{\partial\bar{v}}{\partial\phi} + \frac{\cos\theta}{R\sin\theta}\bar{u}^2\right) + 0.1483\frac{\bar{u}}{\eta}\left(\frac{\bar{u}}{R}\eta_\theta + \frac{\bar{v}}{R\sin\theta}\eta_\phi\right)\right] \\
& + \left[4.0930\frac{1}{R^2}\left(\frac{\partial^2\bar{u}}{\partial\theta^2} + \frac{\cos\theta}{\sin\theta}\frac{\partial\bar{u}}{\partial\theta} - \frac{\cos^2\theta}{\sin^2\theta}\bar{u}\right) + \frac{1}{R^2\sin^2\theta}\frac{\partial^2\bar{u}}{\partial\phi^2}\right. \\
& \quad + 3.0930\frac{1}{R^2\sin\theta}\frac{\partial^2\bar{v}}{\partial\theta\partial\phi} - 5.0930\frac{\cos\theta}{R^2\sin^2\theta}\frac{\partial\bar{v}}{\partial\phi} + 4.8333\frac{\eta_\theta}{R^2\eta}\frac{\partial\bar{u}}{\partial\theta} \\
& \quad + \frac{\eta_\phi}{R^2\eta}\frac{\partial\bar{u}}{\partial\phi} + \frac{\eta_\phi}{R^2\eta\sin^2\theta}\frac{\partial\bar{u}}{\partial\phi} + 1.9167\frac{\eta_\theta}{R^2\sin\theta\,\eta}\frac{\partial\bar{v}}{\partial\phi} + 1.9167\frac{\eta_\phi}{R^2\sin\theta\,\eta}\frac{\partial\bar{v}}{\partial\theta} \\
& \quad + \left(-0.5033\frac{\eta_\phi^2}{R^2\sin^2\theta\,\eta^2} - \frac{\eta_{\phi\phi}}{2R^2\sin^2\theta\,\eta} + 0.1061\frac{\eta_\theta^2}{R^2\eta^2}\right.
\end{aligned}$$

$$-0.5834\frac{\eta_{\theta\theta}}{R^2\eta}+1.4167\frac{\cos\theta}{R^2\sin\theta\,\eta}\eta_\theta\Big)\,\bar u$$
$$+\left(0.6094\frac{\eta_\phi\eta_\theta}{R^2\sin\theta\,\eta^2}-0.0833\frac{\eta_{\theta\phi}}{R^2\sin\theta\,\eta}\ -0.9167\frac{\cos\theta}{R^2\sin^2\theta\,\eta}\eta_\phi\right)\bar v\Big], \quad (83)$$

$$Re\,\frac{\partial\bar v}{\partial t}\approx-\frac{\pi^2}{4}\frac{\bar v}{\eta^2}+\frac{4\bar v}{R\eta}-3.3788\frac{\bar v}{R^2}-\frac{\cos^2\theta}{R^2\sin^2\theta}\bar v$$
$$+Gr\left[\frac{\pi^2}{12}\left(g_\phi+g_n\frac{\eta_\phi}{R\sin\theta}\right)+0.7228\frac{g_\phi\eta}{R}\right]$$
$$+We\,\frac{\pi^2}{12}\left[\frac{2}{R^2}\frac{\eta_\phi}{R\sin\theta}+\frac{1}{R^3\sin^2\theta}\frac{\partial}{\partial\theta}\left(\sin\theta\,\eta_{\theta\phi}\right)+\frac{1}{R^3\sin^3\theta}\eta_{\phi\phi\phi}\right]$$
$$-Re\left[1.3464\frac{\bar u}{R}\frac{\partial\bar v}{\partial\theta}+1.5041\left(\frac{1}{R\sin\theta}\frac{\partial\bar v}{\partial\phi}+\frac{\cos\theta}{R\sin\theta}\bar u\right)\bar v\right.$$
$$\left.+0.1577\,\bar v\frac{\partial\bar u}{\partial\theta}+0.1483\frac{\bar v}{\eta}\left(\frac{\bar u}{R}\eta_\theta+\frac{\bar v}{R\sin\theta}\eta_\phi\right)\right]$$
$$+\Bigg[\frac{1}{R^2}\frac{\partial^2\bar v}{\partial\theta^2}+\frac{\cos\theta}{R^2\sin\theta}\frac{\partial\bar v}{\partial\theta}+4.0930\frac{1}{R^2\sin^2\theta}\frac{\partial^2\bar v}{\partial\phi^2}$$
$$+5.0930\frac{\cos\theta}{R^2\sin^2\theta}\frac{\partial\bar u}{\partial\phi}+3.0930\frac{1}{R^2\sin\theta}\frac{\partial^2\bar u}{\partial\theta\partial\phi}$$
$$+4.8333\frac{\eta_\phi}{R^2\sin^2\theta\,\eta}\frac{\partial\bar v}{\partial\phi}+\frac{\eta_\theta}{R^2\eta}\frac{\partial\bar v}{\partial\theta}+1.9167\frac{\eta_\theta}{R^2\sin\theta\,\eta}\frac{\partial\bar u}{\partial\phi}$$
$$+1.9167\frac{\eta_\phi}{R^2\sin\theta\,\eta}\frac{\partial\bar u}{\partial\theta}$$
$$+\left(-0.5033\frac{\eta_\theta^2}{R^2\eta^2}-\frac{\eta_{\theta\theta}}{2R^2\eta}+0.1061\frac{\eta_\phi^2}{R^2\sin^2\theta\,\eta^2}\right.$$
$$\left.-0.5834\frac{\eta_{\phi\phi}}{R^2\sin^2\theta\,\eta}-\frac{5\cos\theta}{2R^2\sin\theta\,\eta}\eta_\theta\right)\bar v$$
$$+\left(0.6094\frac{\eta_\phi\eta_\theta}{R^2\sin\theta\,\eta^2}-0.0833\frac{\eta_{\theta\phi}}{R^2\sin\theta\,\eta}+4.9167\frac{\cos\theta}{R^2\sin^2\theta\,\eta}\eta_\phi\right)\bar u\Bigg], \quad (84)$$

These models look very complicated, but recall that depending upon the application, simpler truncations are often appropriate; two such examples are (6) and (59). These models have the assurance of centre manifold theory that all physical effects are included to the controllable specified accuracy.

7. Conclusion

We systematically analysed the Navier–Stokes equations for the flow of a thin layer of a Newtonian fluid over an arbitrarily smoothly curved substrate. The resulting general model (57)–(58) resolves the dynamical effects and interactions of inertia, surface tension and a gravitational body force as well as the substrate curvature. We presented evidence towards the end of § 5 that this model applies to flows where the lateral gradients of the fluid thickness are somewhat less than 2, see the more precise limit (62), and (in § 4) where the time scales of the flow are reasonably longer

than the decay of the second lateral shear mode, that is, longer than $0.045\,\eta^2/\nu$. The centre manifold paradigm for dynamical modelling is based upon actual solutions of the governing Navier–Stokes equations, here parameterized in terms of cross-film averaged velocities. Further, the paradigm implicitly arranges the interaction terms between various physical processes to support flexible truncation of the model as appropriate for different parameter regimes; thus, the relatively complex model (57)–(58) may be justifiably simplified as required by your application.

To illustrate a range of applications, we briefly reported some simulations of: two- and three-dimensional wave transitions on a sloping flat plate, Faraday waves on a vibrating flat plate, and a viscous hydraulic jump in radial flow (see § 6.1); the formation and sliding of beads on a cylindrical fibre with surface tension and gravity (see § 6.2); and the generation of vortices in the shear flow between a channel and surrounding shallows (see § 6.3), as well as slow flow up and down smooth steps in the substrate. These simulations demonstrate the resolution of the complex interactions between the varied physical processes encompassed by the model.

We thank the Australian Research Council for a grant to help support this work, and the referees for their many valuable comments.

REFERENCES

Alekseenko, S. V., Markovich, D. M. & Shtork, S. I. 1996 Wave flow of rivulets on the outer surface of an inclined cylinder. *Phys. Fluids* **8**, 3288–3299.

Atherton, R. W. & Homsy, G. M. 1973 Use of symbolic computation to generate evolution equations and asymptotic solutions to elliptic equations. *J. Comput. Phys.* **13**, 45–58.

Atherton, R. W. & Homsy, G. M. 1976 On the derivation of evolution equations for interfacial waves. *Chem. Engng Commun.* **2**, 57–77.

Batchelor, G. K. 1979 *An Introduction to Fluid Dynamics*. Cambridge University Press.

Bohr, T., Ellegaard, C., Hansen, A. E. & Haaning, A. 1996 Hydraulic jumps, flow separation and wave breaking: an experimental study. *Physica* B **228**, 1–10.

Bousmar, D. 2002 Flow modelling in compund channels: momentum transfer between main channel and prismatic and non-prismatic floodplains. PhD thesis, Universitié Catholique de Louvain.

Bousmar, D. & Zech, Y. 2003 Large-scale coherent structures in compound channels. *Tech. Rep.* Universitié Catholique de Louvain.

Burya, A. G. & Shkadov, V. Y. 2001 Stability of a liquid film flowing down an oscillating inclined surface. *Fluid Dyn.* **36**, 671–681, http://dx.doi.org/10.1023/A:1013071331571.

Carr, J. 1981 *Applications of Centre Manifold Theory*. Springer.

Chang, H.-C. 1994 Wave evolution on a falling film. *Annu. Rev. Fluid Mech.* **26**, 103–136.

Chang, H.-C., Demekhin, E. A. & Kopelevich, D. I. 1993 Nonlinear evolution of waves on a vertically falling film. *J. Fluid Mech.* **250**, 433–480.

Chang, H.-C., Demekhin, E. A. & Saprikin, S. S. 2002 Noise-driven wave transitions on a vertically falling film. *J. Fluid Mech.* **462**, 255–283.

Chicone, C. & Latushkin, Y. 1997 Center manifolds for infinite dimensional nonautonomous differential equations. *J. Diffrential Equations* **141**, 356–399.

Cox, S. M. & Roberts, A. J. 1995 Initial conditions for models of dynamical systems. *Physica* D **85**, 126–141.

Decré, M. M. J. & Baret, J.-C. 2003 Gravity-driven flows of viscous liquids over two-dimensional topographies. *J. Fluid Mech.* **487**, 147–166.

Floryan, J. M., Davis, S. H. & Kelly, R. E. 1987 Instabilities of a liquid film flowing down a slightly inclined plane. *Phys. Fluids* **30**, 983–989.

Gallay, T. 1993 A center-stable manifold theorem for differential equations in banach spaces. *Commun. Math. Phys.* **152**, 249–268.

Grotberg, J. B. 1994 Pulmonary flow and transport phenomena. *Annu. Rev. Fluid Mech.* **26**, 529–571.

Guggenheimer, H. W. 1963 *Differential Geometry*. McGraw-Hill.

Howell, P. D. 2003 Surface-tension-driven flow on a moving curved surface. *J. Engng Maths* **45**, 283–308.

Iooss, G. & Peroueme, M.-C. 1993 Perturbed homoclinic solutions in reversible 1 : 1 resonance vector fields. *J. Diffl Equat.* **102**, 62–88.

Jensen, O. E. 1997 The thin liquid lining of a weakly curved cylindrical tube. *J. Fluid Mech* **331**, 373–403.

Kalliadasis, S. & Chang, H.-C. 1994 Drop formation during coating of vertical fibres. *J. Fluid Mech.* **261**, 135–168.

Khayat, R. E., Kim, K.-T. & Delosquer, S. 2004 Influence of inertia, topography and gravity on transient axisymmetric thin-film flow. *Intl J. Numer. Meth. Fluids* **45**, 391–419.

Kheshgi, H. S. 1989 Profile equations for film flows at moderate Reynolds numbers. *AIChE J.* **35**, 1719–1727.

Kliakhandler, I. L., Davis, S. H. & Bankoff, S. G. 2001 Viscous beads on vertical fibre. *J. Fluid Mech.* **429**, 381–390.

Kuznetsov, Y. A. 1995 *Elements of Applied Bifurcation Theory*. Springer.

Lange, U., Nandakumar, K. & Raszillier, H. 1999 Symbolic computation as a tool for high-order long-wave stability analysis of thin film flows with coupled transport processes. *J. Comput. Phys.* **150**, 1–16.

Liu, J., Schneider, J. B. & Gollub, J. P. 1995 Three-dimensional instabilities of film flows. *Phys. Fluids* **7**, 55–67.

Malamataris, N. A., Vlachogiannis, M. & Bontozoglou, V. 2002 Solitary waves on inclined films: flow structure and binary interactions. *Phys. Fluids* **14**, 1082–1094.

Mazouchi, A. & Homsy, G. M. 2001 Free surface stokes flow over topography. *Phys. Fluids* **13**, 2751–2761.

Mei, Z., Roberts, A. J. & Li, Z. 2003 Modelling the dynamics of turbulent floods. *SIAM J. Appl. Maths* **63**, 423–458.

Mercer, G. N. & Roberts, A. J. 1990 A centre manifold description of contaminant dispersion in channels with varying flow properties. *SIAM J. Appl. Maths* **50**, 1547–1565.

Mercer, G. N. & Roberts, A. J. 1994 A complete model of shear dispersion in pipes. *Japan J. Indust. Appl. Maths* **11**, 499–521.

Miles, J. & Henderson, D. 1990 Parametrically forced surface waves. *Annu. Rev. Fluid Mech.* **20**, 143–165.

Moriarty, J. A., Schwartz, L. W. & Tuck, E. O. 1991 Unsteady spreading of thin liquid films with small surface tension. *Phys. Fluids* A **3**, 733–742.

Nguyen, L. T. & Balakotaiah, V. 2000 Modeling and experimental studies of wave evolution on free falling viscous films. *Phys. Fluids* **12**, 2236–2256.

Oron, A., Davis, S. H. & Bankoff, S. G. 1997 Long-scale evolution of thin liquid films. *Rev. Mod. Phys.* **69**, 931–980.

Perlin, M. & Schultz, W. W. 2000 Capillary effects on surface waves. *Annu. Rev. Fluid Mech.* **32**, 241–274.

Prokopiou, T., Cheng, M. & Chang, H. C. 1991 Long waves on inclined films at high Reynolds number. *J. Fluid Mech.* **222**, 665–691.

Pumir, A., Manneville, P. & Pomeau, Y. 1983 On solitary waves running down an inclined plane. *J. Fluid Mech.* **135**, 27–50.

Ramaswarmy, B., Chippada, S. & Joo, S. W. 1996 A full-scale numerical study of interfacial instabilities in thin-film flows. *J. Fluid Mech.* **325**, 163–194.

Ribe, N. M. 2001 Bending and stretching of thin viscous sheets. *J. Fluid Mech.* **433**, 135–160.

Roberts, A. J. 1988 The application of centre manifold theory to the evolution of systems which vary slowly in space. *J. Austral. Math. Soc.* B **29**, 480–500.

Roberts, A. J. 1989 The utility of an invariant manifold description of the evolution of a dynamical system. *SIAM J. Math. Anal.* **20**, 1447–1458.

Roberts, A. J. 1992 A sub-centre manifold description of the evolution and interaction of nonlinear dispersive waves. In *Nonlinear waves* (ed. L. Debnath), chap. 9, pp. 127–156. World Scientific.

Roberts, A. J. 1996 Low-dimensional models of thin film fluid dynamics. *Phys. Letts.* A **212**, 63–72.

Roberts, A. J. 1997 Low-dimensional modelling of dynamics via computer algebra. *Comput. Phys. Commun.* **100**, 215–230.

ROBERTS, A. J. 1998 An accurate model of thin 2d fluid flows with inertia on curved surfaces. In *Free-surface Flows with Viscosity* (ed. P. A. Tyvand), *Advances in Fluid Mechanics Series*, vol. 16, pp. 69–88. Comput. Mech.

ROSKES, G. J. 1969 Three-dimensional long waves on a liquid film. *Phys. Fluids* **13**, 1440–1445.

ROY, R. V., ROBERTS, A. J. & SIMPSON, M. E. 2002 A lubrication model of coating flows over a curved substrate in space. *J. Fluid Mech.* **454**, 235–261.

RUSCHAK, K. J. 1985 Coating flows. *Annu. Rev. Fluid Mech.* **17**, 65–89.

RUSCHAK, K. J. & WEINSTEIN, S. J. 2003 Laminar, gravitationally driven flow of a thin film on a curved wall. *ASME J. Fluids Engng* **125**, 10–17.

RUYER-QUIL, C. & MANNEVILLE, P. 1998 Modeling film flows down inclined planes. *Eur. Phys. J.* B **6**, 277–292.

RUYER-QUIL, C. & MANNEVILLE, P. 2000 Improved modeling of flows down inclined planes. *Eur. Phys. J. B* **15**, 357–369.

SCHWARTZ, L. W. & WEIDNER, D. E. 1995 Modeling of coating flows on curved surfaces. *J. Engng Maths* **29**, 91–103.

SCHWARTZ, L. W., WEIDNER, D. E. & ELEY, R. R. 1995 An analysis of the effect of surfactant on the levelling behaviour of a thin coating layer. *Langmuir* **11**, 3690–3693.

SHKADOV, V. Y. 1967 Wave conditions in the flow of a viscous liquid under the action of gravity. *Izv. Akad. Nauk. SSSR, Mekh. Zhid. Gaza* **1**, 43–50.

SUSLOV, S. A. & ROBERTS, A. J. 1998 Proper initial conditions for the lubrication model of thin film fluid flow. *Tech. Rep.* http://arXiv.org/abs/chao-dyn/9804018.

VLACHOGIANNIS, M. & BONTOZOGLOU, V. 2001 Observations of solitary wave dynamics of film flows. *J. Fluid Mech.* **435**, 191–215.

WATANABE, S., PUTKARADZE, V. & BOHR, T. 2003 Integral methods for shallow free-surface flows with separation. *J. Fluid Mech.* **480**, 233–265.

WATT, S. D. & ROBERTS, A. J. 1995 The accurate dynamic modelling of contaminant dispersion in channels. *SIAM J. Appl. Maths* **55**, 1016–1038.